

ARTICLE

Received 17 Apr 2014 | Accepted 7 Aug 2014 | Published 19 Sep 2014

DOI: 10.1038/ncomms5938

Epidermal photonic devices for quantitative imaging of temperature and thermal transport characteristics of the skin

Li Gao^{1,*}, Yihui Zhang^{2,3,*}, Viktor Malyarchuk^{1,*}, Lin Jia¹, Kyung-In Jang¹, R. Chad Webb¹, Haoran Fu^{2,4}, Yan Shi^{2,5}, Guoyan Zhou^{2,6}, Luke Shi¹, Deesha Shah¹, Xian Huang¹, Baoxing Xu¹, Cunjiang Yu^{7,8}, Yonggang Huang² & John A. Rogers¹

Characterization of temperature and thermal transport properties of the skin can yield important information of relevance to both clinical medicine and basic research in skin physiology. Here we introduce an ultrathin, compliant skin-like, or 'epidermal', photonic device that combines colorimetric temperature indicators with wireless stretchable electronics for thermal measurements when softly laminated on the skin surface. The sensors exploit thermochromic liquid crystals patterned into large-scale, pixelated arrays on thin elastomeric substrates; the electronics provide means for controlled, local heating by radio frequency signals. Algorithms for extracting patterns of colour recorded from these devices with a digital camera and computational tools for relating the results to underlying thermal processes near the skin surface lend quantitative value to the resulting data. Application examples include non-invasive spatial mapping of skin temperature with milli-Kelvin precision (± 50 mK) and sub-millimetre spatial resolution. Demonstrations in reactive hyperaemia assessments of blood flow and hydration analysis establish relevance to cardiovascular health and skin care, respectively.

¹Frederick Seitz Materials Research Laboratory, Department of Materials Science and Engineering, Beckman Institute, University of Illinois at Urbana-Champaign, Urbana, Illinois 61801, USA. ²Center for Engineering and Health, Skin Disease Research Center, Departments of Civil and Environmental Engineering and Mechanical Engineering, Northwestern University, Evanston, Illinois 60208, USA. ³Center for Mechanics and Materials, Tsinghua University, Beijing 100084, China. ⁴Department of Civil Engineering and Architecture, Zhejiang University, Hangzhou 310058, China. ⁵State Key Laboratory of Mechanics and Control of Mechanical Structures, Nanjing University of Aeronautics and Astronautics, Nanjing 210016, China. ⁶Key Laboratory of Pressure Systems and Safety (MOE), School of Mechanical and Power Engineering, East China University of Science and Technology, Shanghai 200237, China. ⁷Department of Mechanical Engineering, University of Houston, Houston, Texas 77204, USA. ⁸Department of Electrical and Computer Engineering, University of Houston, Houston, Texas 77204, USA. * These authors contributed equally to this work. Correspondence and requests for materials should be addressed to J.A.R. (email: jrogers@illinois.edu).

Spatio-temporal imaging of skin temperature offers experimental and investigational value in many areas of medicine, such as for detection of breast cancers and other syndromes, as an adjunctive screening tool to mammography^{1–3}. The required milli-Kelvin levels of precision and millimetre-scale resolution are most commonly achieved by the use of sophisticated infrared digital imaging cameras. However, widespread adoption of such technology is limited by high capital costs, motion artefacts and inability for use outside of clinical or laboratory settings. Other low-cost thermography techniques have been explored for potential screening of deep venous thrombosis^{4–7}, breast cancer^{8–10}, spinal root syndromes^{11,12}, chronic back pain¹³ and even pulmonological diagnostics¹⁴. Recent work^{15,16} demonstrates that electronic temperature-mapping devices can be constructed in ultra-thin, soft and compliant formats, sometimes referred to as ‘epidermal’ due to the similarity of their physical characteristics to those of the skin itself. These systems offer capabilities that bypass many limitations of infrared cameras, but provide only modest spatial resolution and imaging fidelity, limited by multiplexing systems needed to address large sensor arrays. Untethered, wireless operation also demands data transmission components and power sources. Other stretchable smart skin devices that can monitor the vital health signals of the wearer with high levels of function and comfort have been investigated intensively^{15,17–25}.

Here we introduce a simple alternative that combines colorimetric readout and radio frequency (RF) actuation for mapping of thermal characteristics of the skin. The sensors exploit thermochromic liquid crystals (TLC) patterned into large-scale, pixelated arrays on thin elastomeric substrates. Co-integration with electronics provides a means for controlled, local heating by RF signals, to enable not only mapping of temperature but also intrinsic thermal constitutive properties. Uniform layers of TLCs in water-impermeable, non-stretchable thick plastic sheaths, and without electronics, have been explored for skin thermography^{26–28} but without the ability to conform sufficiently well to the curved, textured surface of the skin for accurate, reproducible measurements. Such devices also frustrate transepidermal water loss. They also thermally load the skin and cause irritation at the skin interface, thereby preventing reliable, accurate evaluation or use in continuous modes over long periods of time. Thermochromic textiles are available for cosmetic and fashion purposes^{29–31} but their inability to maintain intimate contact with the skin and the limited capacity to use known thermochromic dyes for precision temperature evaluation prevent their use in the sorts of applications envisioned here. The devices reported in this paper not only avoid these drawbacks but they also allow precise measurement of thermal conductivity and thermal diffusivity through analysis of spatio-temporal images obtained during operation of integrated RF components. Conventional digital cameras and RF transmission systems enable simultaneous readout of thousands of pixels at resolutions that exceed those needed to image temperature and thermal property variations on the skin. The epidermal format induces minimal perturbations on the natural mechanical and thermal properties of the skin. Results presented in the following establish the foundational aspects in materials, mechanics and thermal physics for both electronically active and passive epidermal TLC (e-TLC) devices, including algorithms for extracting precision, calibrated data from colour digital images. Demonstrations in reactive hyperaemia assessments of blood flow, as it relates to cardiovascular health, and hydration analysis, as it relates to skin-care, provide two examples of use in clinically meaningful tests.

Results

Design and fabrication. The e-TLC thermal imagers use a multilayer design that includes a thin (20 μm) black elastomeric membrane as a mechanical support and an opaque background for accurate colorimetric evaluation of the TLC materials; an array of dots of TLC (that is, pixels with 25 μm thicknesses and diameters of either 250 or 500 μm , spaced by 250 or 500 μm), with an optional interspersed array of dots with fixed colours (with 25 μm thicknesses, diameters of 400 μm , spaced by 600 μm) for calibration, both delivered to the surface of the black elastomer by transfer printing; a thin (30 μm) overcoat of a transparent elastomer for encapsulation and optional electronics in thin, stretchable configurations mounted on the back surface for active functionality described subsequently (details appear in Supplementary Fig. 1 and Supplementary Note 1). The TLC material consists of microencapsulated chiral nematic liquid crystals. With increasing temperature, the phase varies from crystalline solid to smectic, cholesteric and, finally, isotropic liquid, all over a range of a few degrees, dictated by the chemistry^{32,33}. In the cholesteric phase, light that reflects from the TLC pixels spans a narrow wavelength range defined by phase coherent interactions with the liquid crystal assemblies. Increases in temperature decrease the pitch, thereby leading to blueshifts in the peak wavelengths of this reflected light. This behaviour provides the basis for colorimetric optical readout. Other phases have no chiral nematic orientation of molecular planes and, thus, do not yield any strong wavelength dependence to the reflection. The small sizes and large spacings of the TLC and calibration pixels, taken together with the low modulus, elastic properties of the substrate, encapsulation layer and electronics, yield soft, compliant mechanics in the overall e-TLC system. These properties yield devices that are well suited for mounting on the skin.

Figure 1a–c shows an e-TLC device on the skin of the forearm when twisted and gently poked with a mildly heated rod. Low interfacial stresses that follow from the low effective modulus and small thickness of the device enable adequate adhesion through van der Waals interactions alone. The collapse of a free-standing device under its own weight, as in Fig. 1c, provides qualitative evidence of these mechanical characteristics. Figure 1d shows a pair of magnified images of e-TLC devices; those on the bottom include interspersed colour calibration pixels consisting of red, green and blue dye in a non-toxic acrylic base (aqueous dispersion of organic pigment and acrylic polymer, Createx). A completed device of this latter type placed on the curved surface of the back of the hand appears in Fig. 1e. As previously mentioned, the backside of the black elastomer substrate provides a mounting location for stretchable electronics. The image in Fig. 1f shows an example of an e-TLC device with a wireless system integrated in this way, for remote delivery of controlled levels of heat. The folded configuration reveals part of the serpentine antenna structure (inset). An illustration of this system, in the form of three-dimensional finite element analysis (3D-FEA), appears in Fig. 1g. The antenna captures incident RF energy to power a Joule heating element (inset, Fig. 1g). The result provides well-defined, localized increases in temperature, as revealed in the pattern of colours in the TLC pixels of Fig. 1h and the infrared images of Fig. 1i. As described subsequently, the results from measurements under such conditions allow determination of the thermal conductivity and thermal diffusivity of the skin.

Mechanical and thermal analysis. A key design goal is to produce e-TLC systems that induce minimal perturbations to the skin, thereby avoiding irritation, enhancing wearability and

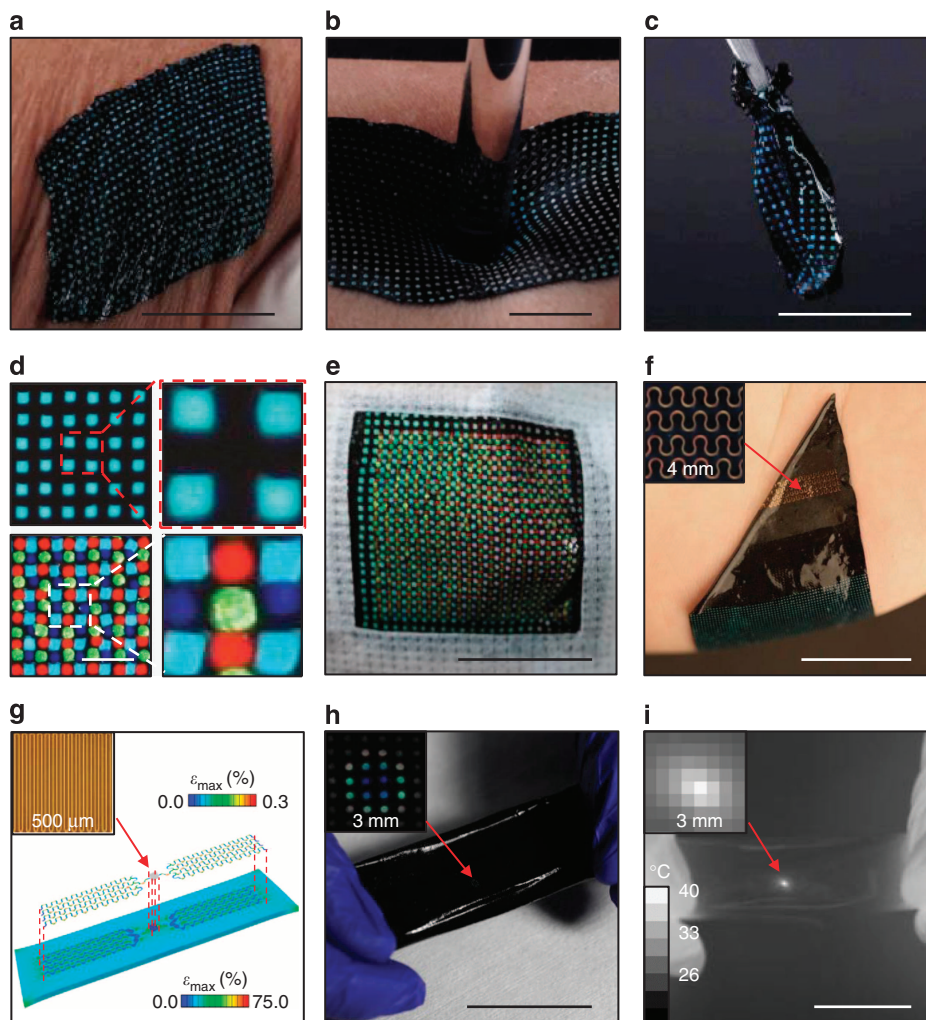


Figure 1 | e-TLC thermal imaging device as an example of an epidermal photonic system. (a) Picture of a device on the skin deformed by pinching in a twisting motion. Scale bar, 3 cm. (b) Picture of a device deformed by poking with a warm glass rod while on the skin. Scale bar, 1 cm. (c) Picture of a device collapsed under its own weight while free-standing. Scale bar, 2 cm. (d) Magnified view of a device operating in the blue region of the spectrum, without and with integrated patterns of dots that have fixed colours for calibration. Scale bar, 2 mm. (e) Picture of a device with calibration colours operating on the curved surface of the skin. Scale bar, 2 cm. (f) Picture of a device that includes a RF antenna and Joule heating element on its back surface, folded over and resting on the palm, with an enlarged view of the serpentine antenna structure (inset). Scale bar, 2 cm. (g) Schematic illustration of finite element modelling results for a device with wireless heater under tensile strain, with magnified view of the Joule heating element (inset). (h) Image of an active, wireless device collected while exposed to RF power in air, with magnified view of the colour changes induced by the heater (inset). Scale bar, 3 cm. (i) Infrared image of the same device under similar conditions, with magnified view in the region of the heater (inset). Scale bar, 3 cm.

ensuring accurate measurement capabilities. The mechanical and thermal properties are particularly important in this context. Experimental and theoretical studies of the former reveal low modulus, elastic characteristics over large ranges of strain. Figure 2a shows the stress/strain responses of an e-TLC device under static uniaxial testing. The results agree well with the predictions of 3D-FEA. In particular, the TLC pixels (~ 221 MPa) and elastomeric substrate (~ 131 kPa) yield an effective modulus (~ 152 kPa and 178 kPa from 3D-FEA and experiment, respectively) that is only slightly larger (by 16–35%) than the intrinsic value associated with the bare elastomer, and is comparable to that of the epidermis itself. The TLC pixels experience ultra-low strain (for example, $<2\%$) even under extreme stretching (for example, 200%), as shown in Fig. 2b. Negligible deformations of the TLC pixels, as observed in experiment and FEA (Fig. 2b), allow approximations for simple, but quantitatively accurate, analytical solutions of the mechanics (see Supplementary Note 2 and Supplementary Fig. 2a). The thicknesses, bending stiffnesses,

effective moduli and stretchability of these devices are $50\ \mu\text{m}$, $3.0\ \text{nN m}$, $178\ \text{kPa}$ and beyond 200%, respectively; these characteristics are superior than those of typical, commercially available TLC sheets (Feverscan, Hallcrest) whose corresponding properties are of $\sim 125\ \mu\text{m}$, $570,000\ \text{nN m}$, $3.3\ \text{GPa}$ and $\sim 5\%$, respectively. The differences are significant at a qualitative level of importance for deployment on the skin. In particular, the collective mechanical characteristics allow largely unconstrained natural motions of the skin, including wrinkling and stretching, even in challenging regions such as the knees and elbows. Addition of calibration pixels reduces the stretchability and increases the modulus (Supplementary Fig. 2b), but retain elastic behaviours at strain levels (50%) that exceed those that can be tolerated by the epidermis (linear response to tensile strain up to 15%, nonlinear to 30% and rupture at $>30\%$ (ref. 34)). Incorporating a wireless electronic heating system further reduces the accessible strain, but with an elastic stretchability of nearly 20%, which is useful for many applications (see

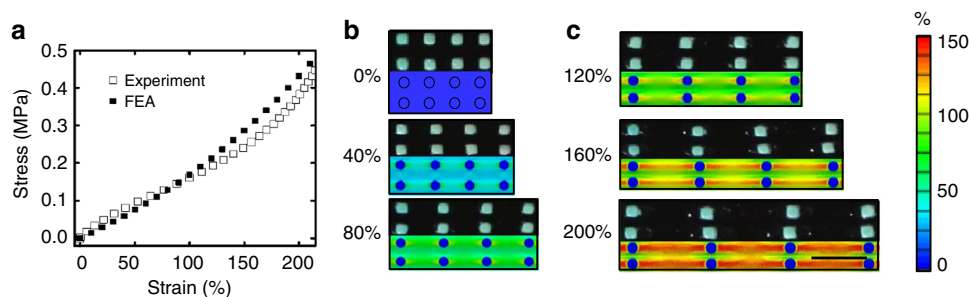


Figure 2 | Mechanical properties of e-TLC devices. (a) Measurements and theoretical calculations of stress-strain responses of a device. (b) Comparison between images and three-dimensional finite element modelling of a representative region of e-TLC device under different levels of tensile strain. Scale bar, 2 mm.

Supplementary Fig. 3)^{35,36}. Although the characteristics of the antenna change with mechanical deformation, experiments indicate that uniaxial stretching (up to 50%) does not disrupt the overall function or the efficiency of power harvesting (see Supplementary Fig. 4); bending can decrease the efficiency. The thermal characteristics of the systems define the thermal load on the skin, as well as the overall time response. For an active e-TLC device, the thermal mass per unit area is $\sim 7.7 \text{ mJ cm}^{-2} \text{ K}^{-1}$ (Supplementary Note 3). This value corresponds to an equivalent of skin with thickness of $\sim 20 \mu\text{m}$, that is, only 25% of the thickness of the epidermis itself³⁷. Water vapour permeability tests on e-TLC and Feverscan strip devices (Supplementary Note 4 and Supplementary Fig. 5) reveals that e-TLC devices provide only minor moisture barrier for operation on the skin. Decreasing the thickness of the device increases the water permeation, as expected (see Supplementary Fig. 5b). Additional increases can be achieved by microstructuring, that is, introducing arrays of holes or pores. The small thermal mass and high water permeability minimize changes in skin temperature and hydration level induced by the presence of the device. Temperatures measured with an infrared camera on the forearm adjacent to an e-TLC and directly underneath it (Supplementary Fig. 6a–c) show minimal differences. The effects of the device on skin hydration (Supplementary Fig. 6d,e) are also small. A mounted 80- μm -thick e-TLC on well-hydrated skin (~ 35) leads to a small percentage increase in hydration (7.5%) after 3 h. For an otherwise identical set of testing conditions, the Feverscan strip led to a $\sim 100\%$ increase in hydration. For monitoring of transient processes, the time response of the system is important. With geometries and materials investigated here, the response time for an e-TLC device is dominated by the thickness and thermal properties of the black elastomer substrate. Transient measurements reveal response times of less than $\sim 30 \text{ ms}$ (Supplementary Note 5), consistent with estimates developed using analytical models (Supplementary Fig. 7). The intrinsic switching times for most TLC materials are $\sim 3\text{--}10 \text{ ms}$ (refs 38–41).

Optical and image analysis. Reflection mode spectroscopic characterization (Zeiss Axio Observer D1) of the steady-state response of the TLC material to changes in temperature between 32°C and 39°C show expected behaviours, as in Fig. 3a. With proper calibration, described next, the temperature extracted from the hue and saturation values determined using a typical digital camera (Canon 5D Mark II) with the e-TLC device held at a nominally constant temperature exhibits an s.d. of $\sim 30 \text{ mK}$ over a measurement time of 760 s. This value is comparable to that observed from temperature readings simultaneously determined with an infrared camera ($\sim 50 \text{ mK}$) (Fig. 3b). The

measurement precision is, then, at least $\pm 50 \text{ mK}$ under these experimental conditions. Equivalent temperatures extracted from analysis of colour recorded at the calibration pixels (red, green and blue) show fluctuations with similar magnitudes, as summarized in Fig. 3c. These observations suggest that the process of image capture and colour analysis enables levels of precision that are comparable to those of infrared cameras, not limited by the physics of the TLC. Detailed calibration plots and information on temperature extraction appear in Supplementary Fig. 8.

Analysis of hue/saturation/value (HSV) data obtained from the digital camera represents the simplest and most straightforward analysis approach. Sophisticated algorithms based on computer vision techniques are advantageous, however, not only for colour determination but for full pixelated analysis of complete e-TLC devices. Figure 3d illustrates an example of a process that exploits computer vision code (OpenCV), in which an image of an e-TLC device that consists of a 7×7 pixel array undergoes a set of colour extraction and data transformation steps (details in Supplementary Note 6). A Gaussian filter first reduces noise through smoothing to yield a grey scale rendering for use with an adaptive threshold that compensates for illumination non-uniformities. The output is a binary mask containing value ‘1’ at bright areas and ‘0’ elsewhere. A two-step erode/dilate process eliminates small speckles that arise from defects. A full list of contours can be extracted from this ‘clean’ image, in which each contour bounds a single pixel in the array. An enclosing circle function uses the contours as inputs to define the pixel positions, for extraction of colour information from the original, unprocessed image. A typical calibration that relates hue and saturation values extracted in this manner to temperature evaluated with an infrared camera appears in Fig. 3e. The biggest advantage of using HSV colour space instead of red/green/blue is that the colour information is encoded only in two (hue and saturation), rather than three (red, green and blue) channels. These two values are comparatively resilient to changes in lighting levels since that information is stored separately in the value channel. Any possible hue/saturation combination can be represented by a point in polar coordinates where radial coordinate corresponds to saturation and angular one to hue. The positions of the calibration set are marked with the dots painted with the corresponding hue. These points define the temperature calibration surface by means of two-dimensional linear fit. The results allow any hue/saturation combination to be assigned to a temperature value, as indicated in the plot using a colour gradient.

Scaled use of this process is summarized in Fig. 3f. Here, a full e-TLC device on a portion of the wrist where near-surface veins are located reveals corresponding variations in temperature of the epidermis. The hue values across the e-TLC yield three-dimensional temperature contour plots that reflect the blood vessels with high spatial resolution (Fig. 3g). A direct comparison

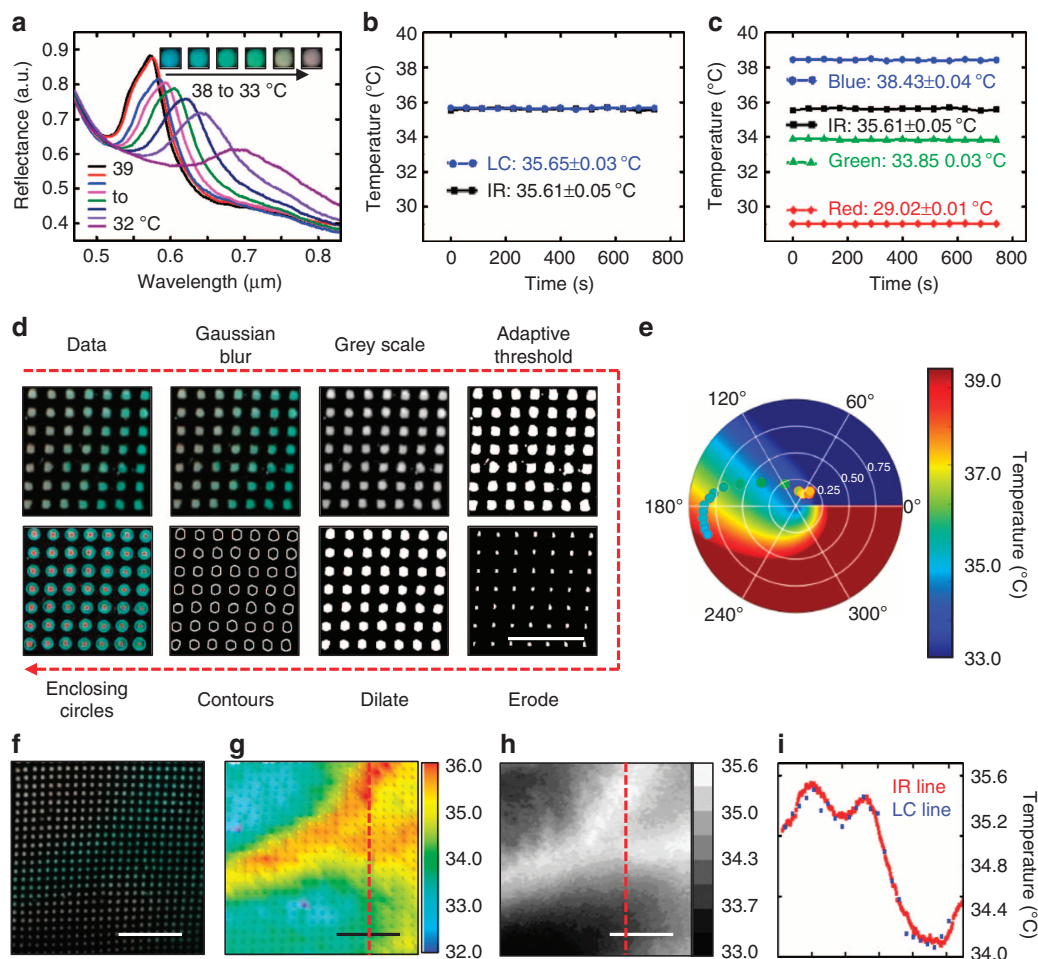


Figure 3 | Calibration and use of e-TLC devices for skin thermal imaging. (a) Reflectance measured at a single pixel from 32 °C to 39 °C and corresponding images for 33 °C to 38 °C (inset). (b) Temporal variations in temperature extracted from digital colour analysis of an e-TLC held, nominally, at a constant temperature. (c) Temporal variations in apparent temperature determined from colour analysis of calibration pixels in an e-TLC device. Frames **b** and **c** also show results obtained with an infrared camera. (d) Illustration of the steps for processing digital images of e-TLC devices, demonstrated on a representative 7 × 7 array of pixels. Scale bar, 5 mm. (e) Colour-temperature calibration determined using hue analysis. (f) Images of an e-TLC device that consists of an 26 × 26 array of pixels, conformally mounted on the wrist. Scale bar, 1 cm. (g) Three-dimensional rendering of the temperature distribution extracted from the colour information obtained by hue value analysis of digital images of the device. Scale bar, 1 cm. (h) Two-dimensional rendering of temperature captured by an infrared camera at the same time and at the same location as in **g**. Scale bar, 1 cm. (i) Line-cut temperature profiles extracted from the data of **g** and **h**.

with temperature distributions measured in the same region with an infrared camera (Fig. 3h) exhibits excellent agreement. Plots of the temperature extracted from these two sets of results at the locations indicated by the dashed red lines in Fig. 3g,h appear in Fig. 3i. These results suggest suitability of e-TLC systems for mapping of vascular distributions in applications such as screening for deep venous thrombosis, without the need for costly infrared camera systems.

In such practical situations, the lighting conditions can strongly affect the precision and accuracy of the temperature determination^{42–45}. In particular, the hue and saturation depend on the type of light source used for illumination. The colour calibration pixels provide a means to compensate for such effects, as their known colours are influenced by the lighting in the same way as the TLC. As a result, it should be possible to develop algorithms that account for shifts in the apparent colours of these calibration pixels and yield a set of numerical compensations that can restore their actual, known colours. Applying the same compensations to the TLC pixels will serve as the basis for a temperature evaluation process that is independent of illumination conditions, within

some reasonable range. Effects of three different lightning conditions appear in Fig. 4. Red, green and blue colour calibration pixels, interspersed across the entire device, are present in this active e-TLC sample. Figure 4a presents an image of the device, with circles that indicate the positions of the TLC pixels. A Joule heating element is present in the centre region. Fluorescent, light-emitting diode and halogen (Fig. 4c–e) light sources provide a range of practical examples. The corresponding temperature calibration data appear in Fig. 4b. The circles correspond to the HSVs of TLC pixels recorded at different temperatures to define calibration fits for specific light sources. The stars delineate the effect of illumination on the colours of the calibration pixels. Red, green and blue calibration pixels are located at ~5°, ~100° and ~240°, respectively. As these colours are known, data from them allow extraction of compensation factors for any given lighting condition. Applying the results to measurements of TLC pixels dramatically reduces the sensitivity of the temperature detection process to the lightning source. Figure 4f presents computed temperatures evaluated along lines that pass through the central region while

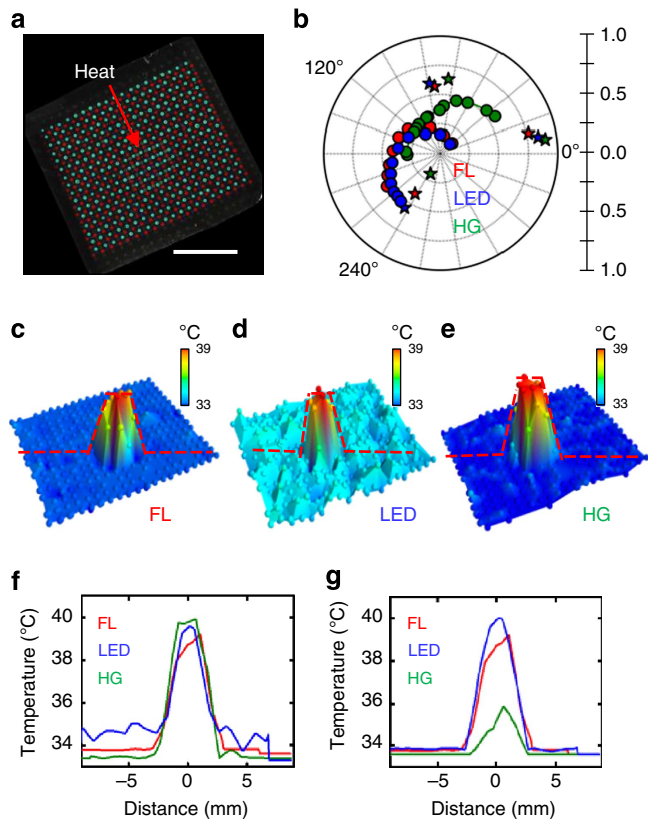


Figure 4 | Temperature analysis under different illumination conditions. (a) Image of a device immediately after local heating at the centre of the array. Scale bar, 1 cm. (b) Hue and saturation values extracted for the calibration (stars) and sensing pixels (dots; red—illumination with a fluorescent light (FL); blue—illumination with a light-emitting diode (LED); green—illumination with a halogen lamp (HG)). Three-dimensional rendering of colour-corrected temperatures determined with (c) white FL, (d) white LED, (e) HG. (f) Line graphs of results collected along the dashed lines shown in c–e. (g) Results similar to those in f, but with fluorescent temperature fit applied to all explored lightning conditions.

the Joule element is activated. The results are comparable for all three lighting sources. To demonstrate the importance of proper calibration, Fig. 4g summarizes data that exploit the fluorescent temperature fit for all lighting conditions explored here. Significant discrepancies occur, as might be expected due to the different colour temperatures of the halogen and light-emitting diode sources; these are reflected not only in the temperature maxima, but also the temperature profiles, shapes and noise levels, all of which again emphasizes the importance of proper calibration and potential for compensation approaches.

Skin thermal property measurements. As suggested by the active e-TLC results in Fig. 4, the local Joule heating element enables additional measurement capabilities. In particular, spatial and temporal variations in temperature at locations near this heater can be used, with thermal models, to extract the thermal conductivity and diffusivity of the skin. Increases in temperature of a few °C can be sufficient for accurate evaluation. The thermal conductivity (k) can be determined by comparing measured steady-state distributions in temperature to axisymmetric thermal conduction models (see Supplementary Note 7). Calculations based on this model suggest spatial decays in

temperature ($T_{\text{sensor-layer}}$) that vary as $1/r$ (except the central sensor), which can be written as

$$T_{\text{sensor-layer}} \approx T_{\infty} + \frac{Q}{2\pi kr}, \quad (1)$$

where r is the distance from the heat source, Q is the heat generated by the Joule heating element and T_{∞} is the temperature of surrounding air. An example appears in Fig. 5a, with details in Supplementary Fig. 9a,b,e. Calibration can be performed through measurements of materials with known properties (Fig. 5b). Figure 5c indicates excellent correspondence between thermal conductivity of the skin evaluated with an active e-TLC and hydration levels determined with a moisture meter (Delfin MoistureMeterSC) that relies on electrical impedance. The quantitative values of k fall within a range that is consistent with literature values determined by subcutaneous thermocouples and high-speed radiometers⁴⁶. By simplifying the heating element as a point heat source that turns on at time $t=0$, the transient temperature variation can be analytically solved as (see Supplementary Note 8)

$$T_{\text{Sensor-layer}}(t) \approx T_{\infty} + \frac{Q}{2\pi kr} \operatorname{erfc}\left(\frac{r}{\sqrt{4\alpha t}}\right), \quad (2)$$

where α is the thermal diffusivity of the skin and $\operatorname{erfc}(x)$ is the complementary error function. Therefore, transient temperature data associated with activation or deactivation of the Joule heating element can be used to determine thermal diffusivity, α , as illustrated in Fig. 5d (see Supplementary Fig. 9a,b,f). As with conductivity, the device can be calibrated using samples with known diffusivity (Fig. 5e). Here, a wireless active e-TLC system serves as the measurement vehicle. The time dependence of the temperature, rather than the absolute values, is sufficient for extraction of diffusivity. The device operates at frequencies of ~ 2 GHz with maximum power inputs of ~ 2.5 W kg⁻¹ for the subject of the studies described here (that is, one-third of the power limit recommended by the Federal Communications Commission's guidelines). The results correspond closely to the hydration level, as shown in Fig. 5f. As with k , the values of α are consistent with literature reports based on techniques such as opto-thermal measurement⁴⁷. The values of k and α can be combined to yield the product of the density (ρ) and heat capacity (c) of the skin, based on the relation ($c\rho = k/\alpha$). The calculations (see Supplementary Fig. 9g) show that the heat capacity increases slightly with hydration level (assuming that ρ is approximately constant), which is consistent with expectation, as the heat capacity (~ 4.2 J g⁻¹ K⁻¹) of water is larger than the human tissue (for example, ~ 3.7 J g⁻¹ K⁻¹ for the dermis and ~ 2.3 J g⁻¹ K⁻¹ for fat)⁴⁸.

Spatio-temporal mapping of reactive hyperaemia test. Spatio-temporal mapping even with passive e-TLC systems yields useful information on blood circulation^{49,50}, maximal percentage increase in blood flow rate after occlusion⁵¹ and duration of reactive hyperaemia⁵². Measurements of temperature fluctuations above the ulnar artery and adjacent veins serve as an important part of a reactive hyperaemia protocol. Here, the flow of blood is temporarily occluded by a pressure cuff on the upper arm, followed by abrupt release. Figure 6a–d summarizes results of measurements performed with an e-TLC device and an infrared camera. Figure 6e presents representative frames of temperature distributions captured at 20 s intervals throughout the experiment. Occlusion, which begins at $t=0$ s, causes the temperature of the skin above the ulnar artery and adjacent areas to decrease drastically, owing to lack of incoming blood flow and loss of heat to the environment. The minimum temperature is achieved at $t=160$ s; at this time, the occlusion is released and

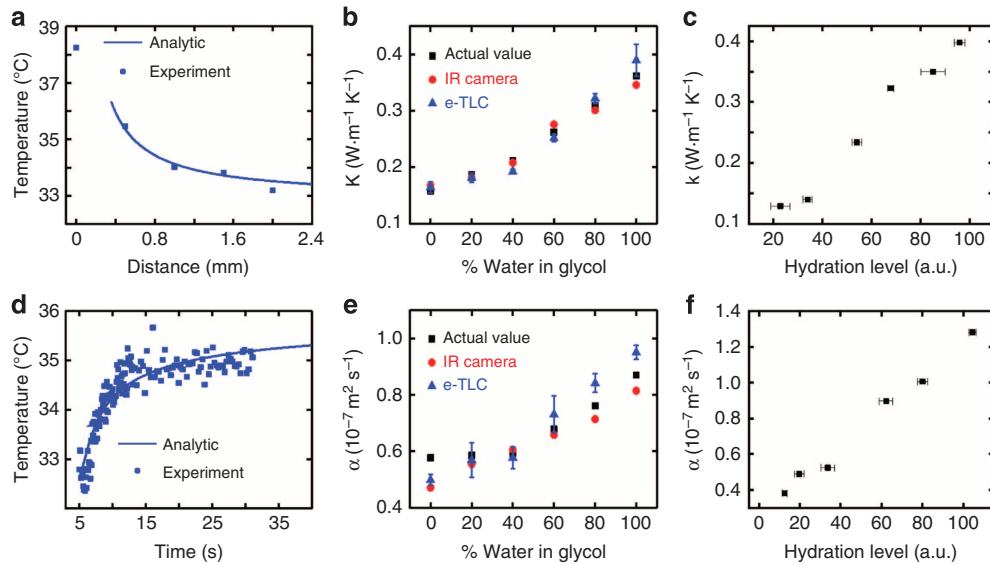


Figure 5 | Determination of skin thermal conductivity and thermal diffusivity. (a) Example of temperatures (symbols) as a function of distance from the position of local heating in an active e-TLC device and corresponding best-fit modelling results (analytic; line) for determining the thermal conductivity. (b) Thermal conductivity of water/ethylene glycol solutions evaluated using an active e-TLC device, and comparison with values obtained from the literature and from analysis of temperatures determined with an infrared camera. The error bars represent average s.d. of measurements obtained with e-TLC, which is $\leq 9\%$. (c) Thermal conductivities measured with an active e-TLC device on the skin at different levels of hydration, separately measured with a commercial moisture meter. The error bars represent average s.d. of measurements obtained with the moisture meter. (d) Example of temperatures (symbols) as a function of time for a location near a wireless heater in an active e-TLC device, and corresponding best-fit modelling results (analytic; line) for determining the thermal diffusivity. (e) Thermal diffusivity of water/ethylene glycol solutions evaluated using an active e-TLC device, and comparison with values obtained from the literature and from analysis of temperatures determined with an infrared camera. The error bars represent average s.d. of measurements obtained with e-TLC, which is $\leq 14\%$. (f) Thermal diffusivities measured with an active, wireless e-TLC device on the skin at different levels of hydration, separately measured with a commercial moisture meter. The error bars represent average s.d. of measurements obtained with the moisture meter.

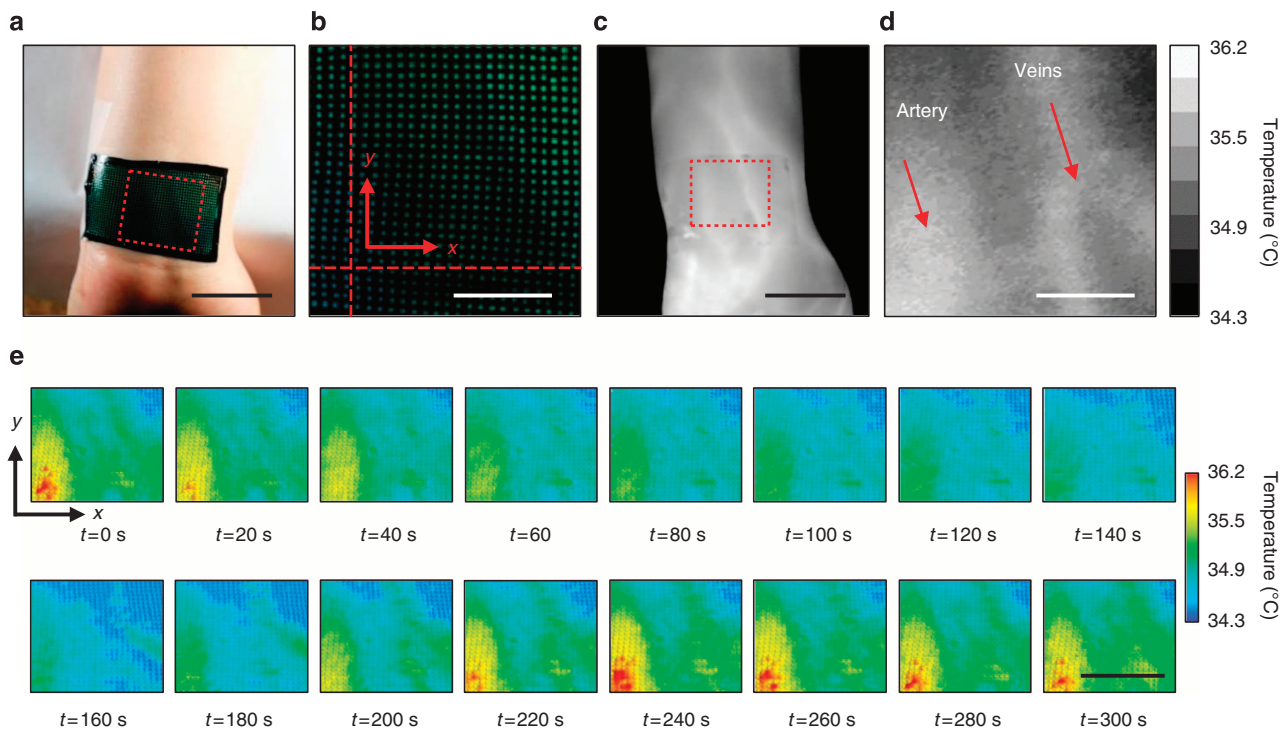


Figure 6 | Application of an e-TLC device in a reactive hyperaemia test. (a) Optical images of an e-TLC device on the wrist during an occlusion test. Scale bar, 3 cm. (b) Magnified view of the device in a. Scale bar, 1 cm. (c) Infrared image of e-TLC device on the wrist. Scale bar, 3 cm. (d) Magnified view of the device in c. Scale bar, 1 cm. (e) Three-dimensional rendering of spatial distributions of temperature determined with the e-TLC device at different times during and after occlusion (occlusion starts at $t=0$ s and ends at $t=160$ s). Scale bar, 2 cm.

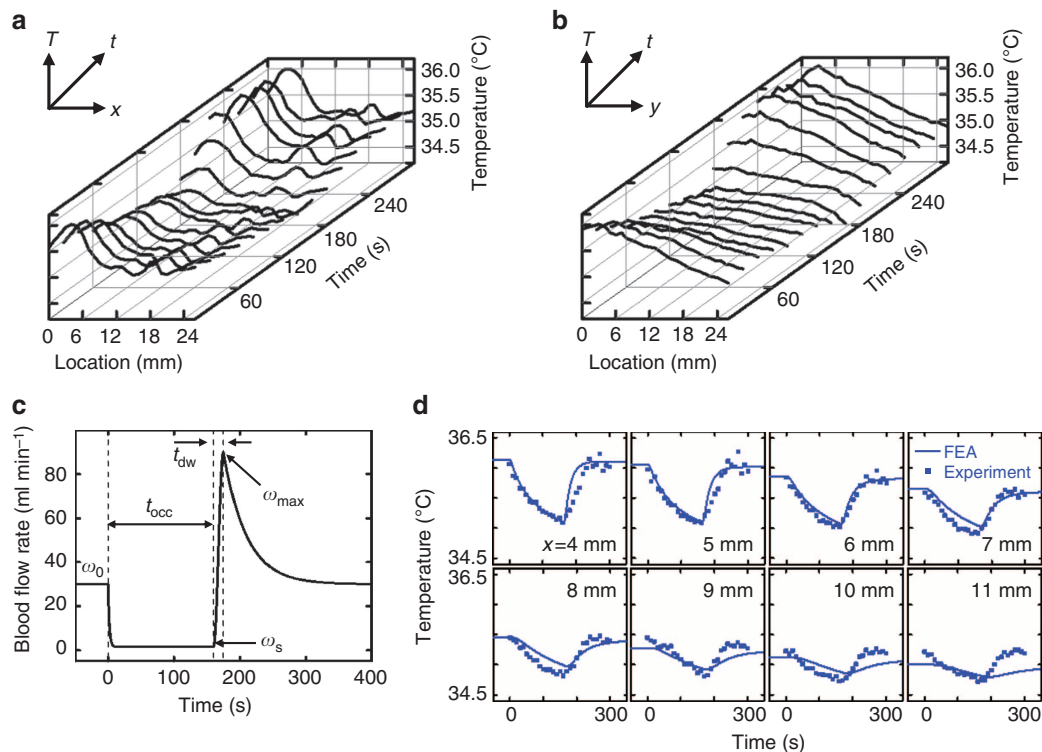


Figure 7 | Study of thermal processes in a reactive hyperaemia test. (a) Line graphs of temperatures along the horizontal dashed red line in Fig. 6b, at various times. (b) Line graphs of temperatures along the vertical dashed red line in Fig. 6b, at various times. (c) Rate of blood flow through the ulnar artery determined by comparison of thermal models with experimental results. The key parameters include: the occlusion time (t_{occ}) = 160 s; time-to-peak-flow (t_{dw}) = 15 s; the baseline flow rate (ω_0) = 30 ml min⁻¹; the occluded flow rate (ω_s) = 1.5 ml min⁻¹; and the peak flow rate (ω_{max}) = 90 ml min⁻¹. (d) Measured temperature rise at the surface of the skin above the ulnar artery during the occlusion along with results from finite element analyses (FEA) using the blood flow rate in frame c. The eight sub-frames correspond to the temperature histories of different points at the horizontal dashed red line in Fig. 6b.

blood flow resumes. Sharp temperature increases occur in areas above the blood vessels, as shown in Fig. 6e, until the temperature stabilizes. The responses of pixels across the array of the e-TLC vary widely depending on their distance from the blood vessels. The maximum temperature fluctuations are $\sim 1.2^\circ\text{C}$ and occur immediately above the ulnar artery; the minimum temperature fluctuations are $\sim 0.4^\circ\text{C}$ and occur at locations away from near-surface blood vessels. Direct comparisons of spatio-temporal variations in temperature obtained from the e-TLC show quantitative agreement with results from an infrared camera (Supplementary Fig. 10). Figure 7a,b highlights temperature variations along horizontal and vertical lines illustrated in Fig. 6b. A thermal model of the human wrist (Supplementary Note 9, Supplementary Tables 1 and 2, and Supplementary Fig. 11) that accounts for both the time-dynamic effect of occlusion and the thermal diffusion from the ulnar artery can capture the effects revealed in the measurements (Fig. 7c,d) and enable extraction of additional physiological information. The temporal variation of blood flow can be described with a piecewise, exponential type function^{53,54}, corresponding to the three stages of the process: pre-occlusion, vascular occlusion and reperfusion. The parameters characterizing this piecewise function can be determined by minimizing the average differences between the temperature-time profiles predicted by the model and those measured by the e-TLC device, during each stage. Figure 7d shows that the calculated temperature history based on the thermal model agrees with experiment at all six of the pixels near the artery (that is, distance < 6 mm). Owing to simplifying assumptions in the models, the FEA does not quantitatively

capture the overshoot behaviour observed in the two nearest sensors. Discrepancies at the two most distant sensors can be attributed to the neglect of heating associated with a nearby vein (~ 13 mm from the artery) in the model. For vessel diameters and depths that lie within reported ranges (Supplementary Note 9), the peak blood flow velocity after occlusion is calculated to be 58.8 cm s^{-1} , representing a threefold increase over the baseline of 19.6 cm s^{-1} , with reactive hyperaemia duration of 144 s. These values match those reported in the literature for a person with low cardiovascular risk^{51,52}.

Epidermal photonic systems, as embodied by the e-TLC devices introduced here, offer strong potential for characterization of the skin and, by extension, important parameters relevant in determining cardiovascular health and physiological status. These same capabilities can be useful in wound treatment and monitoring during a healing process, cancer screening, core body temperature assessments and others of clinical relevance. In all cases, the ability to wear the devices continuously, over days or weeks, and to perform readout and power delivery via a conventional smartphone, represent uniquely enabling features. Photonic operation in the red and near infrared could enable use in near-surface implantable diagnostics.

Methods

Fabrication of e-TLC thermal imaging devices. The fabrication (details in Supplementary Fig. 1) began with spin coating and curing a thin ($20\ \mu\text{m}$) layer of poly(dimethylsiloxane) (PDMS, Sylgard 184, 40:1 mixing ratio) mixed with Iron Oxide Pigment Black 11 (The Earth Pigments Company, LLC) on a substrate of poly(ethyleneterephthalate). A PDMS stamp with arrays of square posts (each post,

0.5 mm × 0.5 mm over an area of 15 cm²; see Supplementary Note 1a) was contacted against a layer of microencapsulated TLC ink (Hallcrest SSN33R5W). Removing the stamp and drying it in air resulted in the formation of a solid layer of TLC material with an average thickness of 25 μm on the raised regions. A thermal release tape (Nitto Denko REVALPHA 90 °C) facilitated transfer of this material from the stamp to the surface of the black PDMS film. The device was completed by spin coating and curing a thin (30 μm) layer of transparent PDMS on top of the structure, as an encapsulant. Fabrication of the wireless heater for the active e-TLC devices began with spin coating of a thin film of polyimide (Sigma Aldrich) on a sacrificial layer of poly(methylmethacrylate) (100 nm, MicroChem) on a silicon wafer. Metal-evaporation (Cr/Au, 5 nm/50 nm), photolithography and wet-etching defined the serpentine structure for the Joule heater. Additional polyimide spin coating, oxygen reactive-ion etching and metal deposition for contacts, interconnects and antenna circuits completed the wireless system. Dissolving the poly(methylmethacrylate) and then physically transferring the electronic structure to the back side of the e-TLC device completed the fabrication.

Device calibration and test for noise level. An e-TLC device was placed on a metal plate with black matt finish on a hotplate. Two white fluorescent light sources were placed on opposite sides of the device for illumination in a manner that avoided specular reflection. A digital camera (Canon Mark II 5D) and an infrared camera (FLIR ExaminIR) placed side-by-side were focused on the same area of the device at a distance of ~30 cm. The angle between the cameras and each of the light sources was ~90°. The device was heated to 40 °C on the hotplate and then the hotplate was turned off. During the cooling process, high-resolution images were collected every 10 s with the digital camera; the infrared camera captured frames at a rate of 12.5 s⁻¹. The process of cooling from 40 °C to 32 °C lasted about 20 min. The colour information of the TLC was extracted from 33 °C to 39 °C with steps of 0.5 °C. The set of algorithms developed to accomplish this task are based on computer vision OpenCV (<http://opencv.org/>) library. The main functions are (in alphabetic order) as follows: 'adaptiveThreshold', 'cvtColor', 'dilate', 'drawContours', 'erode', 'findContours', 'GaussianBlur', 'getStructuringElement', 'imread', 'inRange', 'matchShapes', 'minEnclosingCircle' and 'threshold'. In HSV colour space, the light intensity information is stored in the 'value' channel and is completely separated from the colour information, which is encoded in the 'hue' and the 'saturation' channels. Hue and saturation are, therefore, a natural basis for temperature calibration, as they are not strongly affected by the change in illumination intensity. Temperature calibration was constructed by means of two-dimensional linear fit. The core function used in the process was 'lstsq' from the linear algebra module of Numerical Python (<http://www.numpy.org/>). Any combination of hue/saturation values can be assigned to a temperature value. Even for materials that are not temperature sensitive, such as the calibration colour pixels, their hue/saturation can be treated as a specific temperature for consistency of analysis. To test the noise level and precision of the system, the hotplate temperature was set at a fixed value; temporal fluctuations of TLC colour, calibration dot colour and infrared emission were recorded using the two cameras over a period of 15 min. The colour changes were converted to temperature fluctuation and compared with infrared fluctuation directly.

Reactive hyperaemia test. A volunteer (female, 27 years old) reclined in a chair with her left forearm secured gently to an arm rest using Velcro strips to reduce movement. A pressure cuff was secured around the subject's left bicep. An e-TLC device was placed on the skin of the left wrist approximately above the ulnar artery. Applying puffs of compressed air ensured full, conformal contact. Infrared and digital cameras placed 30 cm above the subject's left wrist were focused on the location of the device while illuminated with white fluorescent lights. The subject was instructed to relax for 5 min. The cuff was inflated to a pressure of 250 mm Hg for 160 s. Continuous high-resolution colour images and infrared temperature measurements were then collected with the two cameras as the occlusion started and was then released. The total duration of the measurement was 300 s. Experiments were conducted with informed consent of human subjects and in accordance with the ethical guidelines of the National Institutes of Health and with the approval of the Institutional Review Board Office of University of Illinois at Urbana-Champaign.

Thermal conductivity/diffusivity and hydration measurements. Thermal conductivity was determined by analysing the spatial distribution of temperature for a few seconds immediately after activation of a Joule heater in an active e-TLC device. To validate the computational models, an active e-TLC device was floated on the surface of a mixture of ethylene glycol/water preheated to ~33 °C. A constant voltage supplied to the e-TLC Joule heating element created a steady-state temperature rise of a few degrees at the location of the heater. Images were then collected with a digital and infrared camera set up above the device with only white fluorescent light sources. The spatial decay of temperature in the e-TLC was recorded by analysis of images from the infrared camera and from colour images of the device. The same experiment was performed on a volunteer's forearm skin. Here, different hydration levels were achieved by applying various amounts of lotion to the measurement location, before application of the active e-TLC device. Immediately after image capture, the e-TLC device was removed and a hydration

meter was used to determine the actual moisture level (averaged from five readings). Measurements of thermal diffusivity used a wireless, active e-TLC, with a transmission antenna located ~10 cm away and adjusted to achieve a peak change in temperature of a few degrees (RF power below 2.5 W kg⁻¹ at frequencies between 1.95 and 2.35 GHz, tuned to match the response of the receiver antenna on the e-TLC). Both digital and infrared cameras were focused on the device with a distance of 30 cm. Videos with 60-s duration recorded the changes in temperature associated with activation and de-activation of the heater. The experiment was validated using the ethylene glycol/water system and then repeated on skin with different hydration levels, in procedures otherwise similar to those for the thermal conductivity measurements.

References

- Arora, N. *et al.* Effectiveness of a noninvasive digital infrared thermal imaging system in the detection of breast cancer. *Am. J. Surg.* **196**, 523–526 (2008).
- Kennedy, D. A., Lee, T. & Seely, D. A comparative review of thermography as a breast cancer screening technique. *Integr. Cancer Ther.* **8**, 9–16 (2009).
- Kerr, J. Review of the effectiveness of infrared thermal imaging (thermography) for population screening and diagnostic testing of breast cancer. *NZHTA Tech. Brief Ser.* **3** (2004).
- Pochaczewsky, R., Pillari, G. & Feldman, F. Liquid crystal contact thermography of deep venous thrombosis. *Am. J. Roentgenol.* **138**, 717–723 (1982).
- Thomas, E. A., Cobby, M. J. D., Davies, E. R., Jeans, W. D. & Whicher, J. T. Liquid-crystal thermography and c-reactive protein in the detection of deep venous thrombosis. *Br. Med. J.* **299**, 951–952 (1989).
- Cameron, E. W., Sachdev, D., Gishen, P. & Martin, J. F. Liquid-crystal thermography as a screening-test for deep-vein thrombosis in patients with cerebral infarction. *Eur. J. Clin. Invest.* **21**, 548–550 (1991).
- Kohler, A., Hoffmann, R., Platz, A. & Bino, M. Diagnostic value of duplex ultrasound and liquid crystal contact thermography in preclinical detection of deep vein thrombosis after proximal femur fractures. *Arch. Orthop. Trauma Surg.* **117**, 39–42 (1998).
- Davison, T. W. *et al.* Detection of breast-cancer by liquid-crystal thermography - preliminary report. *Cancer* **29**, 1123 (1972).
- Pochaczewsky, R. & Meyers, P. H. Vacuum contoured, liquid-crystal, dynamic breast thermoangiography as an aid to mammography in the detection of breast-cancer. *Clin. Radiol.* **30**, 405–411 (1979).
- Bakan, J. A. & Schaab, C. K. Liquid-crystal microcapsule medical device used for the thermographic examination of the human female breast. *Appl. Biochem. Biotechnol.* **10**, 289–299 (1984).
- Pochaczewsky, R. The value of liquid-crystal thermography in the diagnosis of spinal root compression syndromes. *Orthop. Clin. North. Am.* **14**, 271–288 (1983).
- Pochaczewsky, R., Wexler, C. E., Meyers, P. H., Epstein, J. A. & Marc, J. A. Liquid-crystal thermography of the spine and extremities - its value in the diagnosis of spinal root syndromes. *J. Neurosurg.* **56**, 386–395 (1982).
- Newman, R. I., Seres, J. L. & Miller, E. B. Liquid-crystal thermography in the evaluation of chronic back pain - a comparative-study. *Pain* **20**, 293–305 (1984).
- Klosowicz, S. J., Jung, A. & Zuber, J. Liquid-crystal thermography and thermovision in medical applications. Pulmonological diagnostics in *P. Soc. Photo. Opt. Ins.* **4535**, 24–29 (2001).
- Kim, D.-H. *et al.* Epidermal Electronics. *Science* **333**, 838–843 (2011).
- Webb, R. C. *et al.* Ultrathin conformal devices for precise and continuous thermal characterization of human skin. *Nat. Mater.* **12**, 938–944 (2013).
- Sekitani, T. *et al.* A rubberlike stretchable active matrix using elastic conductors. *Science* **321**, 1468–1472 (2008).
- Sekitani, T. *et al.* Organic nonvolatile memory transistors for flexible sensor arrays. *Science* **326**, 1516–1519 (2009).
- Mannsfeld, S. C. B. *et al.* Highly sensitive flexible pressure sensors with microstructured rubber dielectric layers. *Nat. Mater.* **9**, 859–864 (2010).
- Tee, B. *et al.* An electrically and mechanically self-healing composite with pressure- and flexion-sensitive properties for electronic skin applications. *Nat. Nanotech.* **7**, 825–832 (2012).
- Kaltenbrunner, M. *et al.* An ultra-lightweight design for imperceptible plastic electronics. *Nature* **499**, 458–463 (2013).
- Schwartz, G. *et al.* Flexible polymer transistors with high pressure sensitivity for application in electronic skin and health monitoring. *Nat. Commun.* **4**, 1859 (2013).
- Wang, C. *et al.* User-interactive electronic-skin for instantaneous pressure visualization. *Nat. Mater.* **12**, 899–904 (2013).
- Xu, S. *et al.* Soft Microfluidic Assemblies of Sensors, Circuits, and Radios for the Skin. *Science* **344**, 70–74 (2014).
- Son, D. *et al.* Multifunctional wearable devices for diagnosis and therapy of movement disorders. *Nat. Nanotech.* **9**, 397–404 (2014).
- Brull, S. J. *et al.* Comparison of crystalline skin temperature to esophageal temperatures during anesthesia. *Anesthesiology* **73**, A472 (1990).

27. Ikeda, T. *et al.* Influence of thermoregulatory vasomotion and ambient temperature variation on the accuracy of core-temperature estimates by cutaneous liquid crystal thermometers. *Anesthesiology* **86**, 603 (1997).
28. Wisniewski, C. M. A comparison of esophageal temperature readings and liquid crystal temperature readings in the pediatric population. CRNA Masters Thesis, Virginia Commonwealth Univ. (1991).
29. Aitken, D. *et al.* Textile applications of thermochromic systems. *Rev. Prog. Coloration* **26**, 1–8 (1996).
30. Chowdhury, M. A. *et al.* Application of thermochromic colorants on textiles: temperature dependence of colorimetric properties. *Color. Technol.* **129**, 232–237 (2012).
31. Chowdhury, M. A. *et al.* Photochromic and thermochromic colorants in textile applications. *J. Eng. Fiber. Fabr.* **9**, 107–123 (2014).
32. Dolphin, D., Muljiani, Z., Cheng, J. & Meyer, R. B. Low-temperature chiral nematic liquid-crystals derived from beta-methylbutylaniline. *J. Chem. Phys.* **58**, 413–419 (1973).
33. Sage, I. Thermochromic liquid crystals. *Liquid Crystals* **38**, 1551–1561 (2011).
34. Arumugam, V., Naresh, M. D. & Sanjeevi, R. Effect of strain-rate on the fracture-behavior of skin. *J. Biosci.* **19**, 307–313 (1994).
35. Davis, J. R. *ASM Specialty Handbook: Copper and Copper Alloys* (ASM International, 2001).
36. William, F. R., Leroy, D. S. & Don, H. M. *Mechanics of Materials* (Jon Wiley & Sons, 1999).
37. Sandby-Moller, J., Poulsen, T. & Wulf, H. C. Epidermal thickness at different body sites: relationship to age, gender, pigmentation, blood content, skin type and smoking habits. *Acta. Derm. Venereol.* **83**, 410–413 (2003).
38. Kakade, V. U., Lock, G. D., Wilson, M., Owen, J. M. & Mayhew, J. E. Accurate heat transfer measurements using thermochromic liquid crystal. Part 1: calibration and characteristics of crystals. *Int. J. Heat. Fluid Fl.* **30**, 939–949 (2009).
39. Stasiek, J. A. & Kowalewski, T. A. Thermochromic liquid crystals applied for heat transfer research. *Opto. Electron. Rev.* **10**, 1–10 (2002).
40. Rao, Y. & Zang, S. Calibrations and the measurement uncertainty of wide-band liquid crystal thermography. *Meas. Sci. Technol.* **21**, 015105 (2010).
41. Ireland, P. T. & Jones, T. V. The response-time of a surface thermometer employing encapsulated thermochromic liquid-crystals. *J. Phys. E. Sci. Instrum.* **20**, 1195–1199 (1987).
42. Farina, D. J., Hacker, J. M., Moffat, R. J. & Eaton, J. K. Illuminant invariant calibration of thermochromic liquid-crystals. *Exp. Therm. Fluid. Sci.* **9**, 1–12 (1994).
43. Anderson, M. R. & Baughn, J. W. Liquid-crystal thermography: illumination spectral effects. Part 1 - Experiments. *J. Heat. Trans. T. Asme.* **127**, 581–587 (2005).
44. Sabatino, D. R., Praisner, T. J. & Smith, C. R. A high-accuracy calibration technique for thermochromic liquid crystal temperature measurements. *Exp. Fluids* **28**, 497–505 (2000).
45. Kodzwa, Jr P. M. & Eaton, J. K. Angular effects on thermochromic liquid crystal thermography. *Exp. Fluids* **43**, 929–937 (2007).
46. Cohen, M. L. Measurement of the thermal-properties of human-skin. A review. *J. Invest Dermatol.* **69**, 333–338 (1977).
47. Xiao, P., Cui, Y., Ciorte, L. I., Berg, E. P. & Imhof, R. E. Opto-thermal in-vivo skin hydration measurements – a comparison study of different measurement techniques. *J. Phys. Conf. Ser.* **214**, 012026 (2010).
48. Fiala, D., Lomas, K. J. & Stohrer, M. A computer model of human thermoregulation for a wide range of environmental conditions: the passive system. *J. Appl. Physiol.* **87**, 1957–1972 (1999).
49. Holowatz, L. A., Thompson-Torgerson, C. S. & Kenney, W. L. The human cutaneous circulation as a model of generalized microvascular function. *J. App. Physiol.* **105**, 370–372 (2008).
50. Gorbach, A. M. *et al.* Infrared imaging of nitric oxide-mediated blood flow in human sickle cell disease. *Microvasc. Res.* **84**, 262–269 (2012).
51. Huang, A. L. *et al.* Predictive value of reactive hyperemia for cardiovascular events in patients with peripheral arterial disease undergoing vascular surgery. *Arterioscl. Throm. Vasc.* **27**, 2113–2119 (2007).
52. Ishibashi, Y. *et al.* Short duration of reactive hyperemia in the forearm of subjects with multiple cardiovascular risk factors. *Circ. J.* **70**, 115–123 (2006).
53. Akhtar, M. W., Kleis, S. J., Metcalfe, R. W. & Naghavi, M. Sensitivity of digital thermal monitoring parameters to reactive hyperemia. *J. Biomech. Eng. T. Asme.* **132**, 051005 (2010).
54. Deshpande, C. *Thermal Analysis of Vascular Reactivity*, MS Thesis, Texas A&M Univ. (2007).

Acknowledgements

This study was supported by the Materials Research Laboratory and Center for Micro-analysis of Materials at the University of Illinois at Urbana-Champaign. J.A.R. acknowledges financial support through a National Security Science and Engineering Faculty Fellowship. The work was supported by the Office of Naval Research under Grant N00014-10-1-0989.

Author contributions

L.G., L.J., C.W. and J.A.R. designed the experiments. L.G., K.J., X.H., B.X., C.Y. and J.A.R. designed the device layouts. L.G., L.S. and D.S. carried out the fabrication. L.G., V.M., Y.Z., L.J. and J.A.R. carried out experimental validation and data analysis. Y.Z., H.F., Y.S., G.Z. and Y.H. contributed to the thermal modelling and mechanical modelling of strain. L.G., Y.Z., V.M., Y.H. and J.A.R. co-wrote the paper.

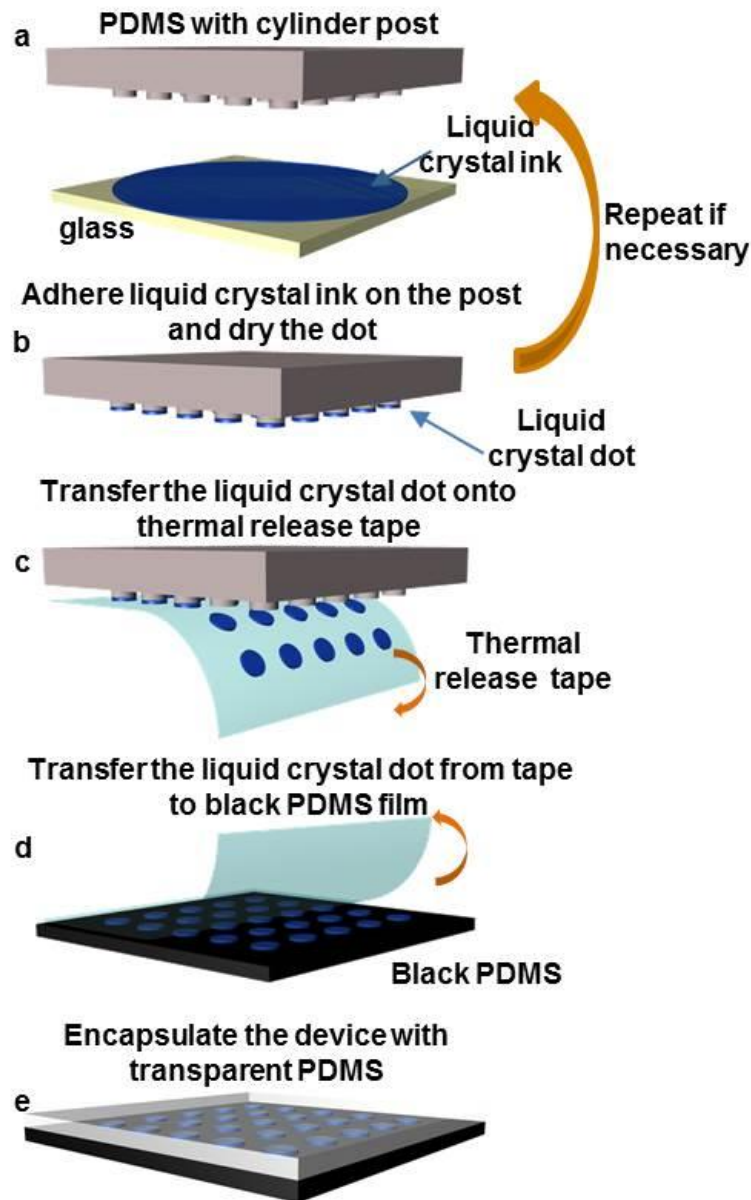
Additional information

Supplementary Information accompanies this paper at <http://www.nature.com/naturecommunications>

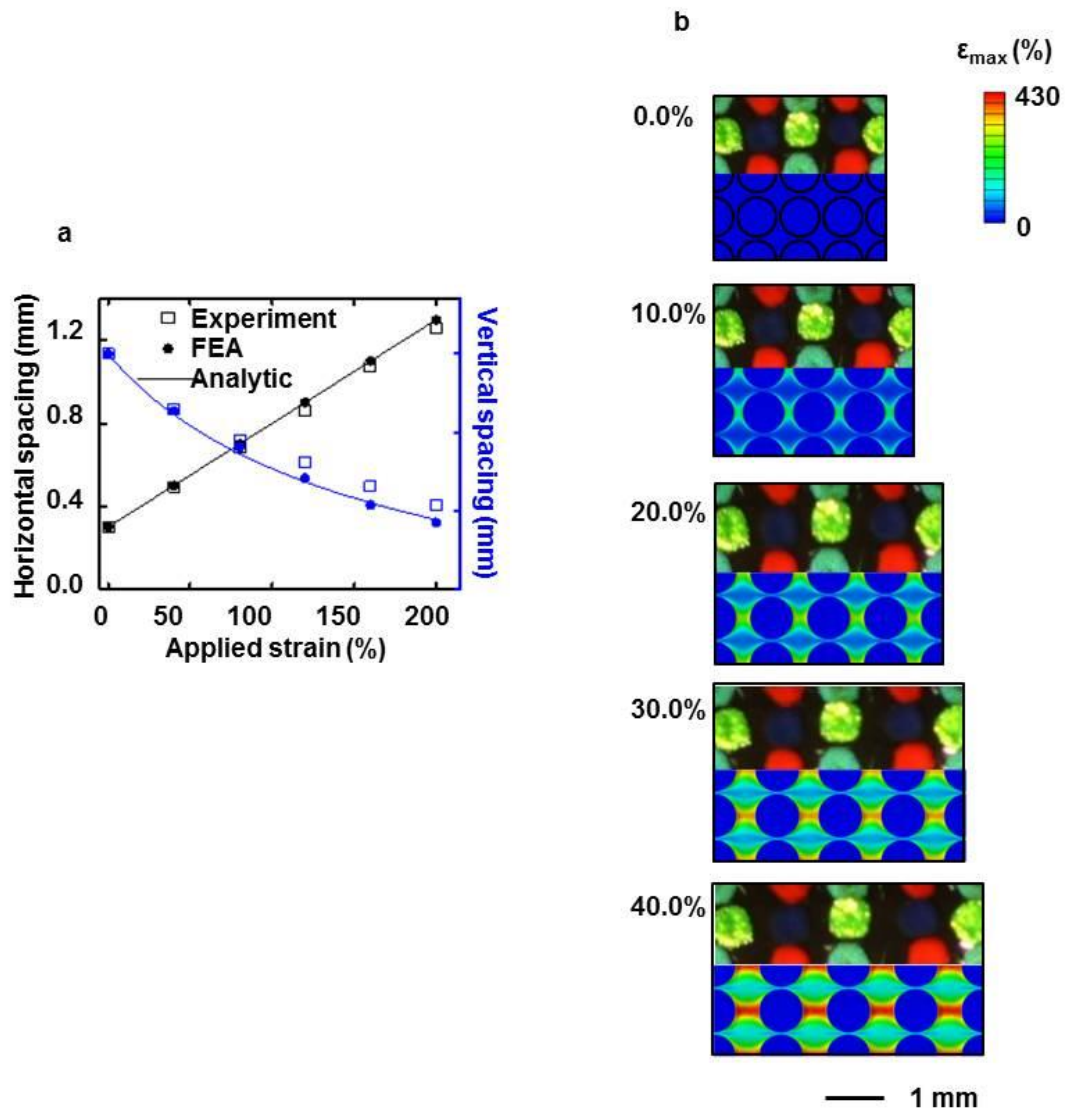
Competing financial interests: The authors declare no competing financial interests.

Reprints and permission information is available online at <http://npg.nature.com/reprintsandpermissions/>

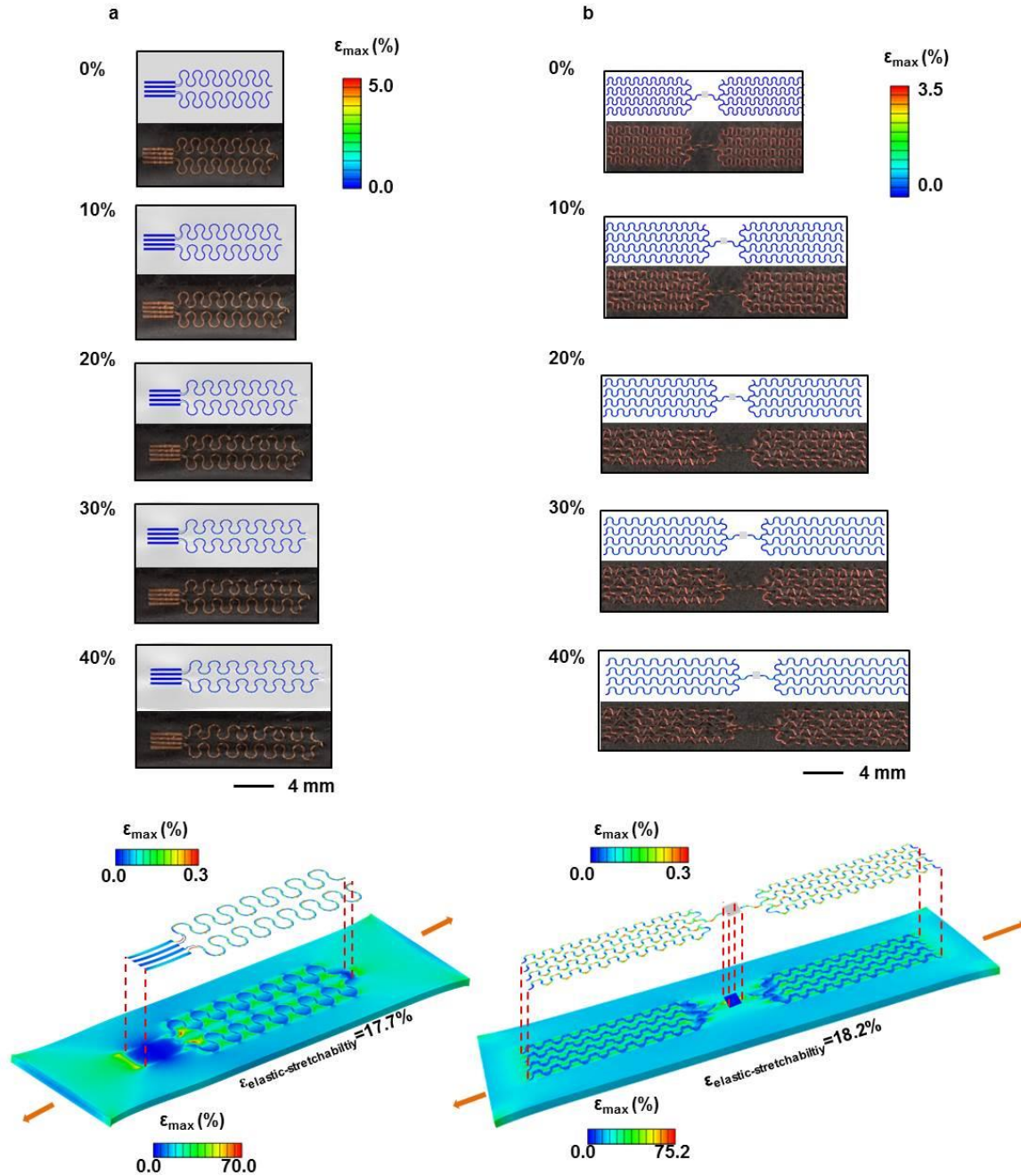
How to cite this article: Gao, L. *et al.* Epidermal photonic devices for quantitative imaging of temperature and thermal transport characteristics of the skin. *Nat. Commun.* **5**:4938 doi: 10.1038/ncomms5938 (2014).



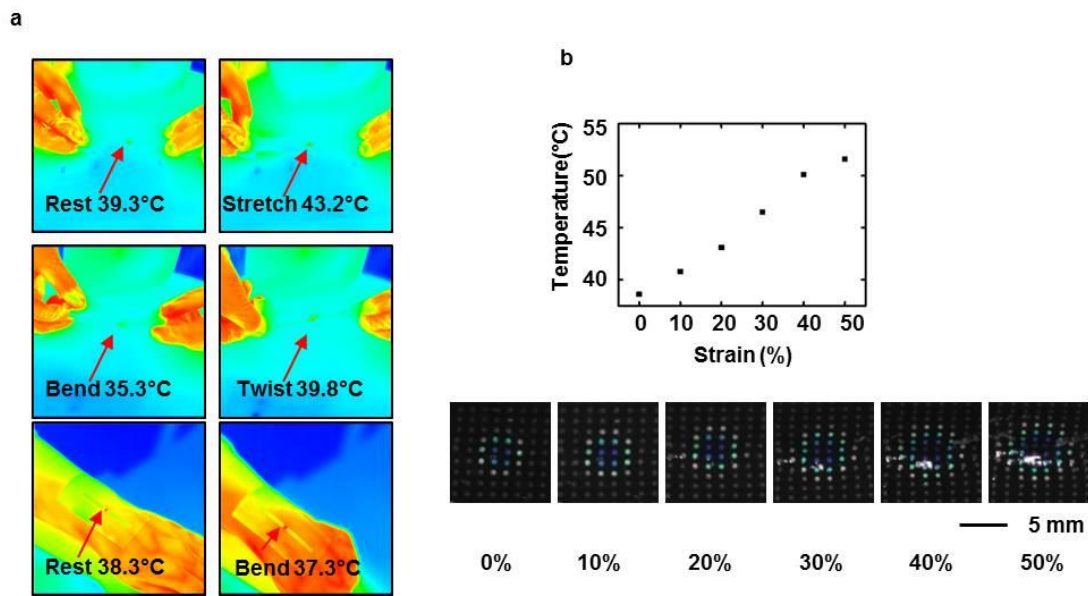
Supplementary Figure 1: Process for fabricating e-TLC devices. (a) A PDMS stamp with an array of posts embossed on its surface is ‘inked’ by bringing it into contact with a uniform layer of TLC aqueous slurry spin cast on a glass slide while still in wet state. The thickness of the ink was $\sim 100\ \mu\text{m}$ to ensure that the ink contacts on the top surfaces of the posts. (b) The inked TLC material on the PDMS stamp was allowed to dry in air for 15 minutes. The thickness of the dried film is $\sim 15\ \mu\text{m}$. Additional ‘inking’ processes are repeated to achieve a final thickness of $25\text{-}30\ \mu\text{m}$. A typical TLC pixel is thickest in the center due to the hydrophobic nature of the PDMS surface and the large contact angle formed during the inking process. (c) Transfer printing allows delivery of the TLC to a piece of thermal release tape. (d) Transfer to the black PDMS substrate is enabled by heat activated release from the tape. (e) The device is encapsulated with a transparent layer of PDMS by spin casting.



Supplementary Figure 2: Mechanical response of an e-TLC device to uniaxial strain. (a) Experimental, analytical and finite element modeling results for the change in horizontal and vertical spacings between adjacent pixels under different levels of tensile strain. (b) Comparison between images and three dimensional finite element modeling of a representative region of an e-TLC device that incorporates color calibration pixels under different levels of tensile strain.

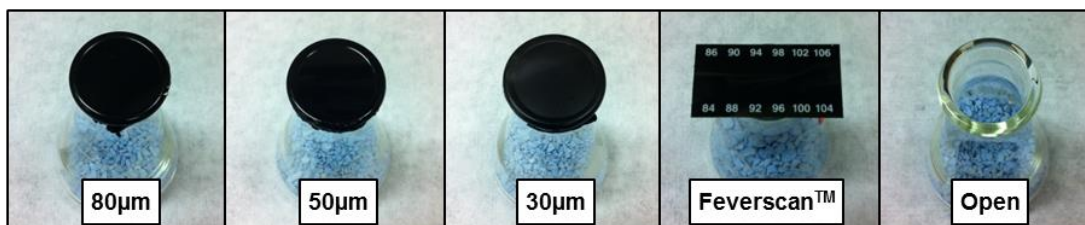


Supplementary Figure 3: Experimental and computational studies of the mechanical properties of Joule heater element. (a) Comparison between experimental images and three dimensional finite element modeling of a wired Joule heating element under different levels of tensile strain, and strain distribution computed for the case of stretching to 50%. (b) Comparison between experimental images and three dimensional finite element modeling of a wireless Joule heater under different levels of tensile strain, and strain distribution computed for the case of stretching to 50%.

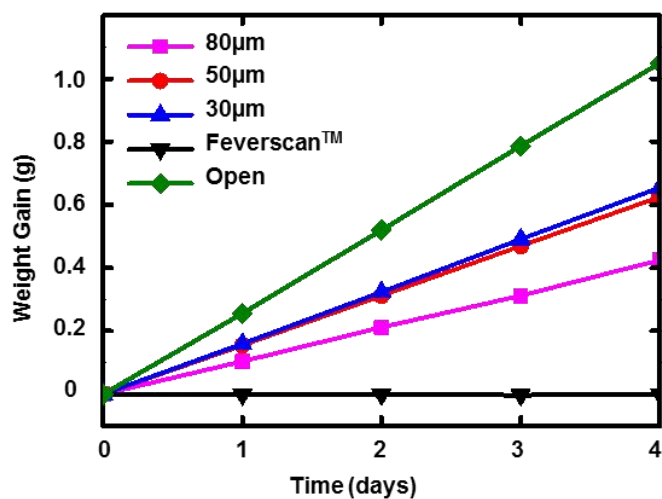


Supplementary Figure 4: Experimental studies of the effect of strain on the efficiency of wireless Joule heating. (a) Infrared temperature measurements for a wireless Joule heater under exposure to RF energy while mechanically deformed in different ways, both in air and on skin. (b) Measurements at different levels of tensile strain with corresponding images.

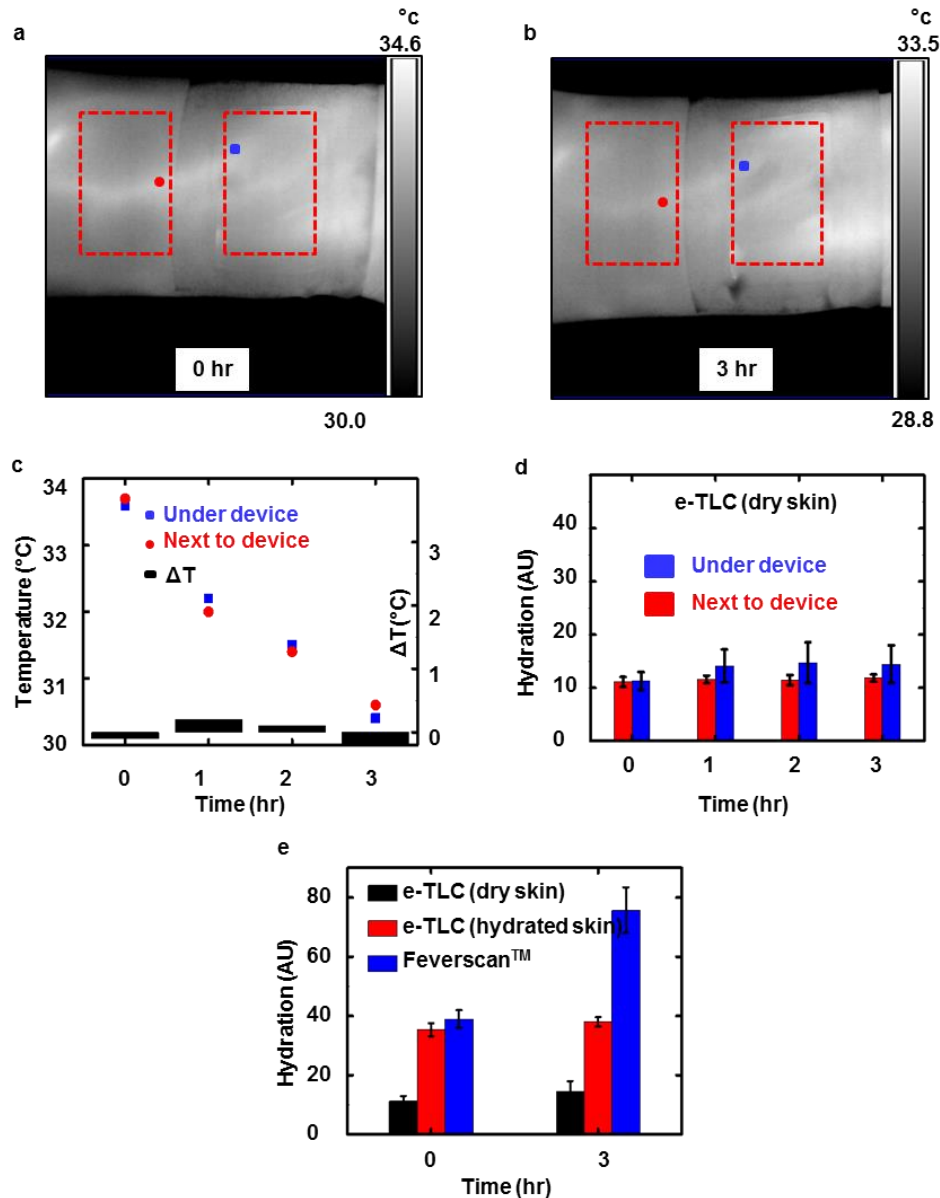
a



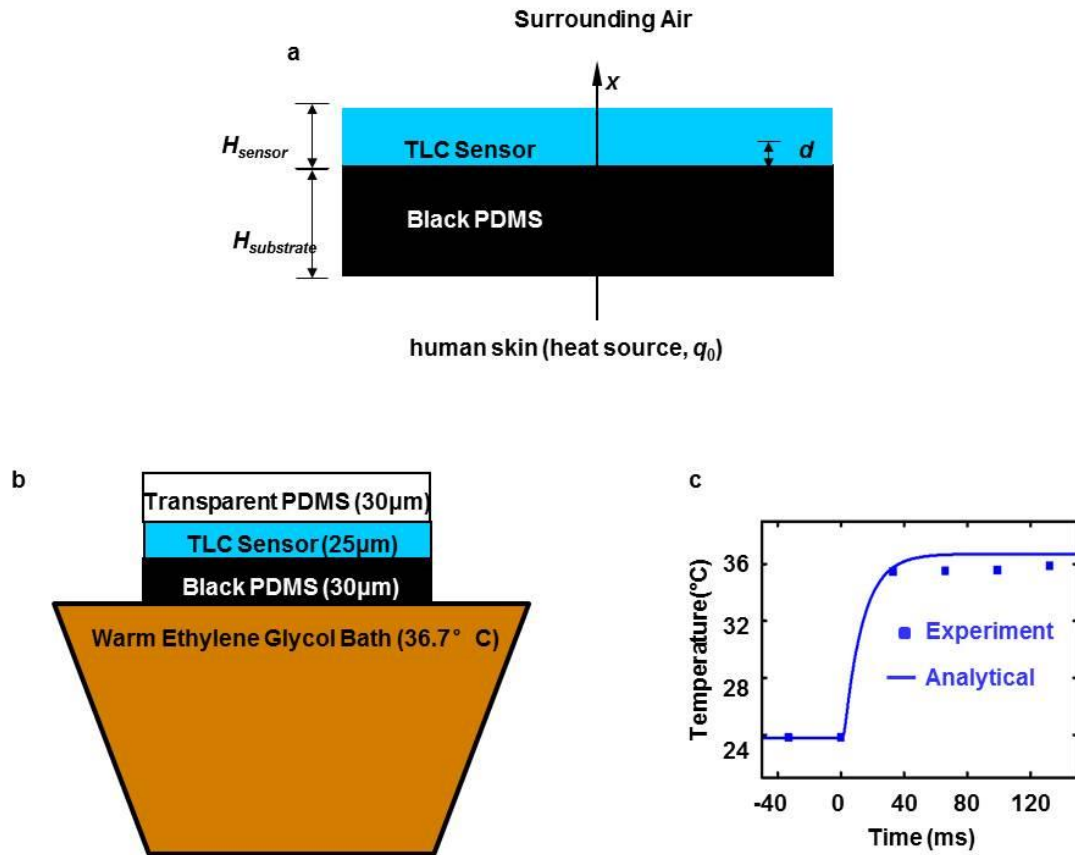
b



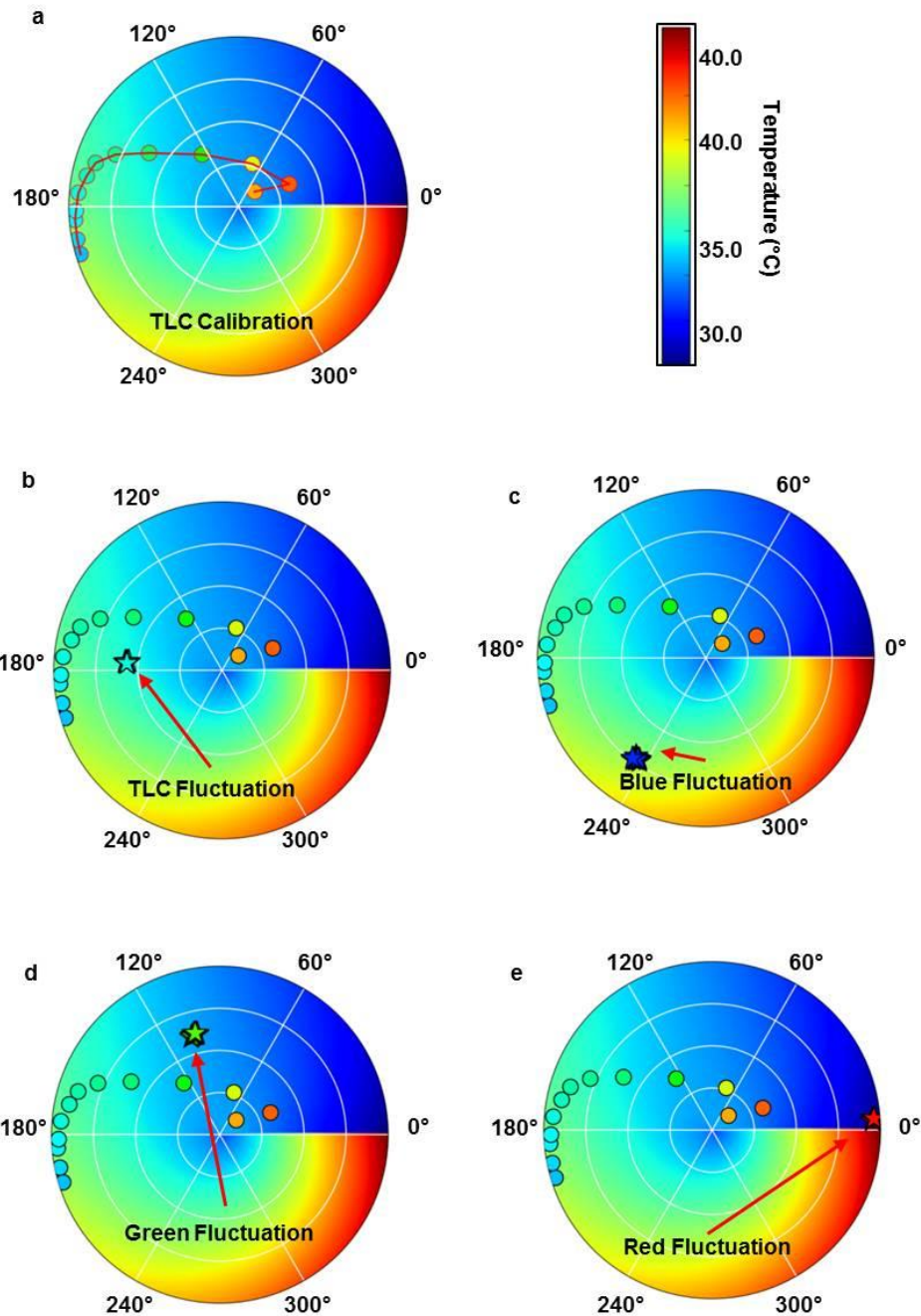
Supplementary Figure 5: Water permeability test. (a) Images of the experimental set-ups for measurement of water permeation according to ASTM E96-95 guidelines, and (b) Results of the change in weight as a function of time associated with water uptake by the desiccant, for e-TLC devices with different thicknesses and for a commercial TLC strip.



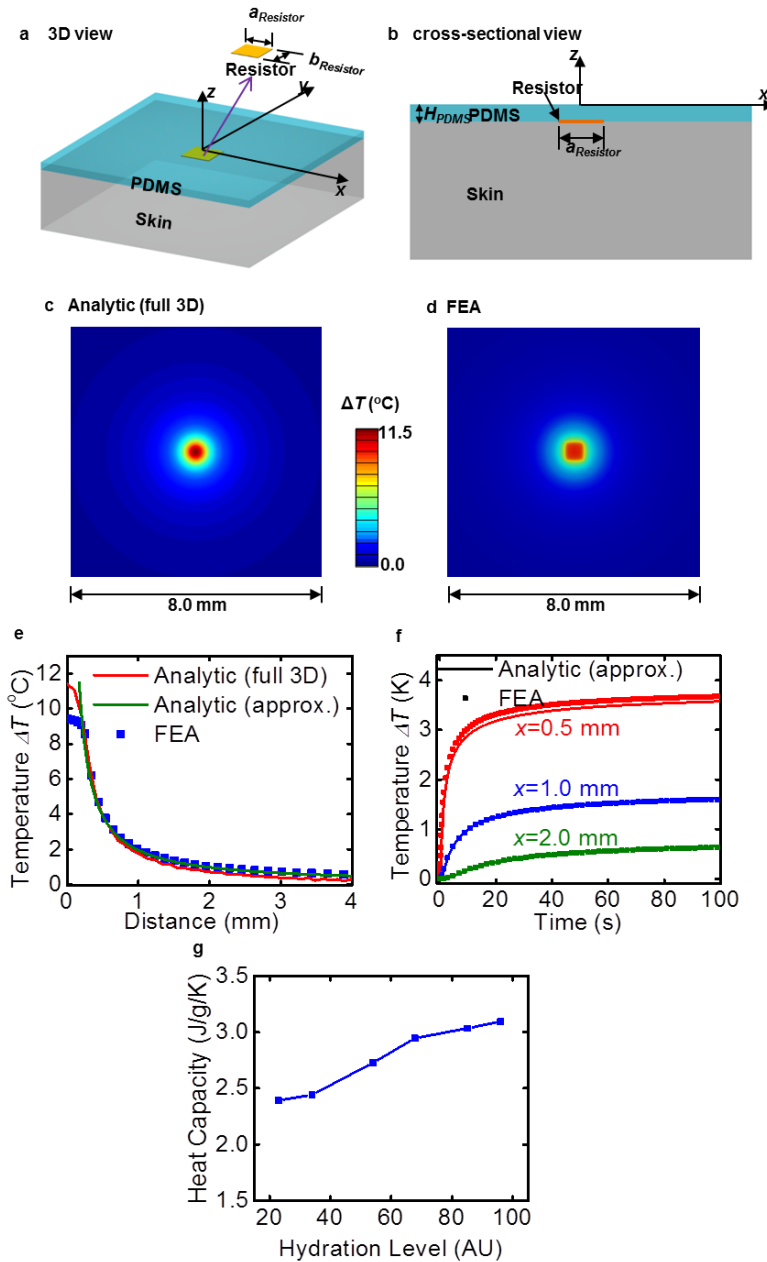
Supplementary Figure 6: Effect of e-TLC operation on temperature and hydration of the skin. (a) Infrared image captured immediately after mounting an e-TLC device on the wrist. (b) Infrared image captured 3 hours after mounting. For both (a) and (b), the data indicate that the average temperatures at the regions of the device are the same as those adjacent to the device. (c) Temperature difference between a point near the device and a point underneath the device shows no obvious increase during the three hour operation. (d) Measurement of hydration using a Delfin meter in a region of dry skin (baseline reading ~10) after 3 hours of contact with an 80 μm thick e-TLC indicates an increase of ~25%. (e) The same device, under identical conditions, on well hydrated skin (baseline reading ~35) leads to much smaller percentage increases (7.5%). For an otherwise identical set of testing conditions, the Feverscan™ strip led to a ~100% increase in the hydration.



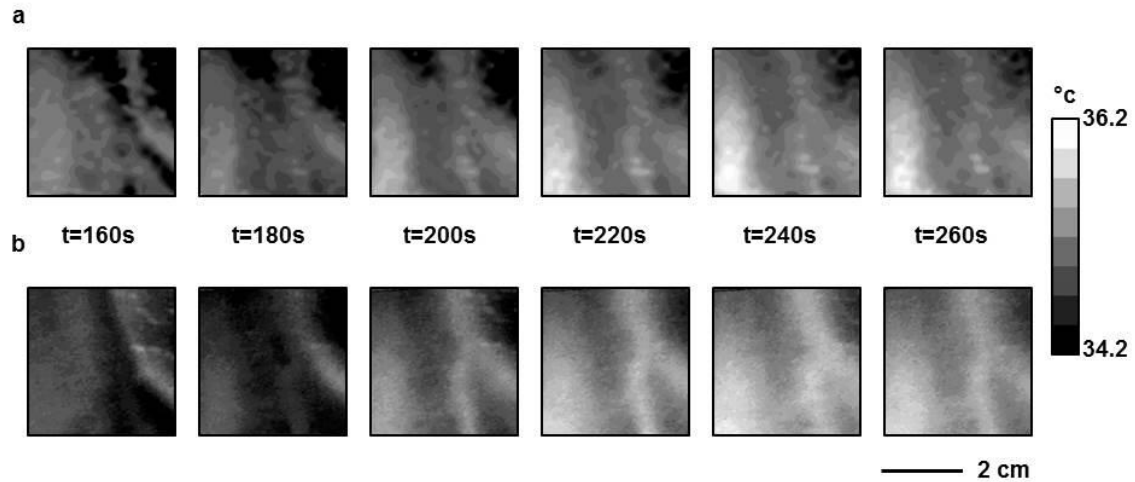
Supplementary Figure 7: Sensor response time. (a) Layers used in analytical modeling to determine sensor response time on skin. (b) Experimental setup for measuring sensor response time. A warm ethylene glycol bath, which has similar thermal properties to skin, is in contact with the e-TLC device from the back surface. (c) Experimental sensor response time captured by high speed camera, and corresponding analytic predictions based on a one-dimensional heat conduction model. In experiment, the time required for the sensor to reach 90% of the total temperature change is achieved in one frame which is approximate 33 ms for the case of 30 μm black PDMS and 25 μm liquid crystal.



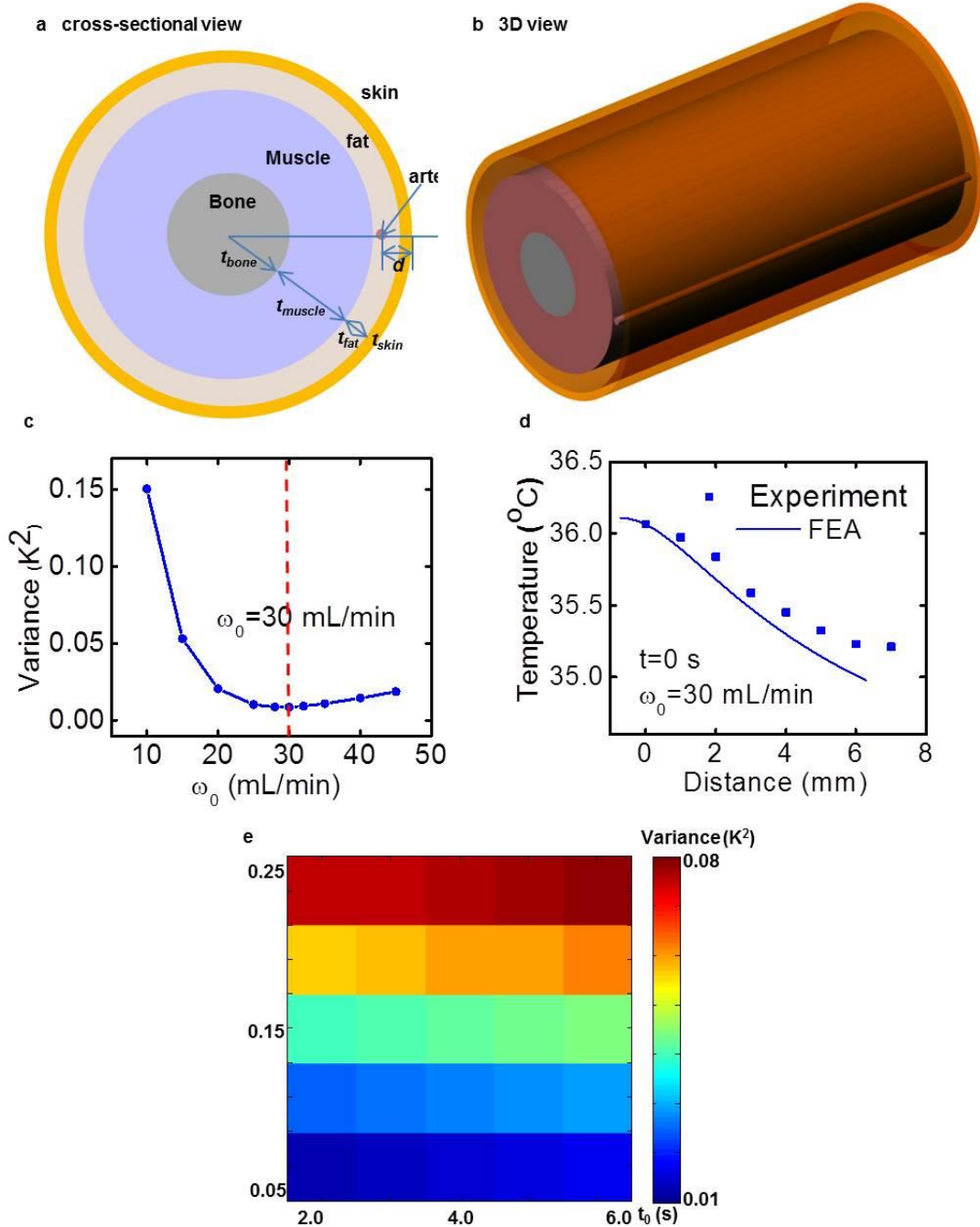
Supplementary Figure 8: Noise and uncertainty examined using temperature insensitive acrylic colors. (a) TLC color-temperature calibration plotted in the hue/saturation space. Symbols are located at positions corresponding to the hue/saturation values of the TLC during calibration runs, as indicated with their hue values. Temperatures are calculated with a two dimensional linear fit and are represented by a color gradient. (b) Temporal fluctuation in the color of the TLC, when held at a nominally fixed temperature. (c) Temporal fluctuation of the blue calibration color at fixed temperature. (d) Temporal fluctuation of the green calibration color at fixed temperature. (e) Temporal fluctuation of the red calibration color at fixed temperature.



Supplementary Figure 9: Finite element models that allow determination thermal conductivity and diffusivity from data collected using active e-TLC devices. (a) A 3D view of a model with a Joule heater embedded between an e-TLC device and the skin. (b) A cross-sectional view of a model with a Joule heater embedded between an e-TLC device and the skin. (c) Analytical model of the spatial decay in temperature at steady state during operation of the Joule heater. (d) Corresponding finite element modeling results. (e) Analytical and finite element model of the spatial temperature decay with a wired Joule heater operation along one dimension. (f) Analytical and finite element model of the temporal temperature rise with a wireless Joule heater operation for locations away from the heater. (g) Skin heat capacity inferred from the skin thermal conductivity and diffusivity values in Figure 5.



Supplementary Figure 10: Comparison of an e-TLC thermal imaging device and infrared camera measurement in a reactive hyperaemia test. (a) Spatial distributions of temperature determined with the e-TLC device at representative times from t=160s to t=260s at an interval of 20s. **(b)** Spatial distributions of temperature determined with the infrared camera at representative times from t=160s to t=260s at an interval of 20s.



Supplementary Figure 11: Schematic illustration of the thermal conduction model that determines the blood flow rate during occlusion. (a) Cross-sectional view and (b) three-dimensional view of the wrist model; (c) Temperature variance of FEA and experiment versus the baseline flow rate; (d) Experimental results of the steady-state temperature as a function of the distance from the artery, as compared to the FEA calculations using the baseline flow rate of 30 mL/min; (e) Distribution of temperature variance in the space of parameters, α and τ_0 , during stage II of occlusion.

Supplementary Table 1. The parameter range in the model of reactive hyperemia for simulations.

	ω_0 (mL/min)	$\alpha=\omega_s/\omega_0$	$\beta=\omega_{max}/\omega_0$	T_0 (s)	t_{dw} (s)	T_h (s)
Range	[10, 45]	[0.05, 0.25]	[3, 10]	[2, 6]	[15, 45]	[35, 75]

Supplementary Table 2. The geometric and thermal-physical properties of various tissues for the wrist, where t denotes the thickness, D is the diameter of the artery, and d is the depth of the artery.

Parameter	Skin	Fat	Muscle	Bone	Blood
ρ (kg/m ³) ^(2,4)	1085	850	1085	1357	1069
c_p (J/kg/K) ^(2,4)	3680	2300	3768	1700	3659
k (W/m/K) ^(5,7)	0.47	0.16	0.42	0.75	/
t (mm) ⁽⁵⁻⁷⁾	1.0	4.4	13.6	10.0	/
D (mm) ⁽⁸⁾	/	/	/	/	1.8
d (mm) ^(9,10)	/	/	/	/	2.2

Supplementary Note 1:

Fabrication procedure for PDMS post stamp used for inking liquid crystal

1. Clean a 3" Si wafer (Acetone, IPA -> Dry 5 min at 110 °C).
2. Spin coat SU8 50 (microchem, 1000rpm for 30s, anneal 65°C 10min 95°C 30min)
3. Pattern SU8 with 365nm optical lithography through iron oxide mask (Karl Suss MJB3) develop in SU8 developer
- 4 post exposure bake at 65°C 1min 95°C 10min
5. STS ICP RIE silicon etch SF6 20s at 20w CF4 10s at 0w for 250cycles to achieve a hole depth of around 400um
6. Mold the silicon template with PDMS

Fabrication procedure for a single heater with wired and wireless design

Prepare polymer base layers

1. Clean a 3" Si wafer (Acetone, IPA -> Dry 5 min at 110 °C).
2. Spin coat with PMMA (poly(methyl methacrylate), spun at 3,000 rpm for 30 s).
3. Anneal at 180 °C for 10 min.
4. Spin coat with polyimide (PI, poly(pyromellitic dianhydride-co-4,4' -oxydianiline), amic acid solution, Sigma-Aldrich, spun at 4,000 rpm for 30 s for wired design and 1,000 rpm for 30s for wireless design).
5. Anneal at 110 °C for 30 s.
6. Anneal at 150 °C for 5 min.
7. Anneal at 250 °C under vacuum for 1 hr.

Deposit first metallization

8. E-beam 5/50 nm Cr/Au.
9. Pattern photoresist (PR; Clariant AZ5214, 3000 rpm, 30s) with 365 nm optical lithography through iron oxide mask (Karl Suss MJB3).
Develop in aqueous base developer (MIF 327).
10. Etch Au with TFA Au etchant (Transene).
11. Etch Cr with CR-7 Cr Mask Etchant (Cyantek).
12. Remove PR w/ Acetone, IPA rinse.
13. Dry 5 min at 150 °C.

Isolate first metallization and pattern via holes

14. Spin coat with PI.
15. Anneal at 110 °C for 30 s.
16. Anneal at 150 °C for 5 min.
17. Anneal at 250 °C under vacuum for 1 hr.
18. Pattern photoresist (PR; Clariant AZ4620, 3000 rpm, 30s;) with 365 nm optical lithography through iron oxide mask (Karl Suss MJB3). Develop in aqueous base developer (AZ 400K, diluted 3:1).
19. Reactive ion etch (RIE; March CS-1701, 50 mTorr, 20 sccm O₂, 150 W, 35 min).

Deposit second metallization

20. E-beam 5/500 nm Cr/Au for wired design or 5/1600nm Cr/Cu for wireless design.
21. Pattern PR AZ5214.
22. Etch Au with TFA Au etchant or etch Cu with TFA Cu etchant.cs
23. Etch Cr with Cr Mask Etchant.

24. Remove PR w/ Acetone, IPA rinse.

25. Dry 5 min at 150 °C.

Isolate entire device

26. Spin coat with PI.

27. Anneal at 110 °C for 30 s.

28. Anneal at 150 °C for 5 min.

29. Anneal at 250 °C under vacuum for 1 hr.

30. Pattern PR AZ4620.

31. RIE (50 mTorr, 20 sccm O₂, 150 W, 35 min for wired design and 120 min for wireless design).

Release and transfer

32. Release w/ boiling Acetone.

33. Transfer to water soluble tape.

34. E-beam 3/30 nm Ti/SiO₂.

35. Transfer to back of e-TLC device.

36. Bond thin, flexible cable (Elform, HST-9805-210) using hot iron with firm pressure for wired heater

Supplementary Note 2: Analytic solution of spacing of e-TLC dots during uniaxial stretching

The deformation of an e-TLC device under uniaxial stretching (along horizontal direction) is analyzed to determine the change of spacing between pixels associated with the applied strain (ϵ). The e-TLC material (~221 MPa) is much

stiffer than the elastomeric substrate (~131 kPa), and therefore undergoes negligible deformation, as evidenced by the experiment images of FEA results in Fig. 2b. The stretching deformation is, as a result, mainly accommodated by the soft substrate material. For pixels (in diameter of d_{TLC}) with an initial spacing Δ_0 , the horizontal spacing ($\Delta_{horizontal}$) after deformation is given by

$$\Delta_{horizontal} = \Delta_0 + (\Delta_0 + d_{TLC}) \varepsilon. \quad (1)$$

The vertical spacing ($\Delta_{vertical}$) decreases due to the Poisson effect. For sparsely distributed pixels (e.g., $d_{TLC} < \Delta_0$), the mechanical constrains associated with the e-TLC on the transverse compression can be neglected, such that the vertical spacing ($\Delta_{vertical}$) after deformation can be approximated as

$$\Delta_{vertical} = \frac{\Delta_0 + d_{TLC}}{\sqrt{1 + \varepsilon}} - d_{TLC}. \quad (2)$$

Note that the transversely compressive strain of the soft substrate, due to stretching (ε), is given by $\varepsilon_{compression} = 1 - (1 + \varepsilon)^{-1/2}$, since it is nearly incompressible (i.e., Poisson ratio $\nu=0.5$). For $\Delta_0 = 0.3$ mm, $d_{TLC} = 0.2$ mm, as adopted in experiments, the analytic results in Fig. S2a, based on Eqs. (S1) and (S2), agree well with the experiment and FEA results.

Supplementary Note 3: Thermal mass calculation of e-TLC device

The thermal mass of the devices are determined for 20 μm silicone and black iron oxide substrate and 30 μm transparent silicone substrate. The devices have an overall aerial coverage of ~15 cm^2 . The calculated thermal masses that follow

are given as thermal mass per unit area of skin. The device construction for the TCR device contains approximately $8.7 \text{ ng}\cdot\text{cm}^{-2}$ of Au, $56 \text{ }\mu\text{g}\cdot\text{cm}^{-2}$ of PI, $55.8 \text{ }\mu\text{g}\cdot\text{cm}^{-2}$ of Cu, $0.64 \text{ mg}\cdot\text{cm}^{-2}$ of black iron oxide powder, $4.18 \text{ mg}\cdot\text{cm}^{-2}$ of silicone substrate, $\sim 0.61 \text{ mg}\cdot\text{cm}^{-2}$ of liquid crystal materials (Hallcrest, density $0.97\text{g}\cdot\text{cm}^{-3}$). The material contributions to aerial thermal mass are: $21.48 \text{ }\mu\text{J}\cdot\text{cm}^{-2}\cdot\text{K}^{-1}$ from Cu, $64.4 \text{ }\mu\text{J}\cdot\text{cm}^{-2}\cdot\text{K}^{-1}$ from PI, $0.42 \text{ mJ}\cdot\text{cm}^{-2}\cdot\text{K}^{-1}$ from black iron oxide, $\sim 1.09 \text{ mJ}\cdot\text{cm}^{-2}\cdot\text{K}^{-1}$ from liquid crystal (Hallcrest, specific heat $1.8 \text{ J}\cdot\text{g}^{-1}\cdot\text{K}^{-1}$), $6.11 \text{ mJ}\cdot\text{cm}^{-2}\cdot\text{K}^{-1}$ from the silicone backing (calculate values) and negligible from Au. This results overall device aerial thermal masses of $\sim 7.7 \text{ mJ}\cdot\text{cm}^{-2}\cdot\text{K}^{-1}$. The thermal mass of skin depends on the water content where thermal mass increases with skin hydration and water content². For hydrated skin, the heat capacity is approximately $3.7 \text{ J}\cdot\text{cm}^{-3}\cdot\text{K}^{-1}$, and the device aerial thermal mass of $7.7 \text{ mJ}\cdot\text{cm}^{-2}\cdot\text{K}^{-1}$ is equivalent to the aerial thermal mass of skin with a thickness of $20.8 \text{ }\mu\text{m}$.

Supplementary Note 4: Water vapor permeability test

Water permeability tests followed the ASTM E96 - 95 standard, and involved evaluation of e-TLC devices (thicknesses of $80 \text{ }\mu\text{m}$, $50 \text{ }\mu\text{m}$ and $30 \text{ }\mu\text{m}$) and a commercial FeverscanTM device (LCR Hallcrest; polyester covering film $\sim 75\mu\text{m}$, liquid crystal layer $\sim 10\text{-}50\mu\text{m}$, black backing layer $\sim 10\text{-}20\mu\text{m}$ and graphic print layer $\sim 10\text{-}20\mu\text{m}$). The experiments involved sealing the tops of identical jars, each containing a fixed amount of desiccant (97% anhydrous calcium sulfate and 3% cobalt chloride), with the devices under test. Control samples consist of jars without any seal on top. Diffusion of water vapor through the devices from the

surrounding ambient air causes increases in weight, due to uptake by the desiccant. All jars were placed in a room that has consistent temperature ($\sim 22^{\circ}\text{C}$) and humidity ($\sim 50\%$). The weight gain of each jar was recorded at the same time of day on a balance that has precision of 0.1mg. By this test, after a 4-day period, the weight of the jar sealed by the FeverscanTM remains unchanged, consistent with negligible water permeation. By contrast, weight of the jar with the 80 μm e-TLC device increases by an amount that is nearly half (41%) of that compared to the control. The 50 μm and 30 μm e-TLC devices exhibit weight increases that are greater than half of the control, i.e. 60% and 62%, respectively. These results indicate that our formulation of PDMS, at the thicknesses used in our devices, provide only minor barriers to moisture, particularly when compared to conventional analogs.

Supplementary Note 5: Sensor response time

The TLC dot array is embedded in between two PDMS layers. The thickness and thermal properties of the black PDMS substrate and the TLC layer will both determine the heat transfer rate from the skin to the top of TLC layer. The effect from the top encapsulation elastomer is neglected to simplify the model.

A warm ethylene glycol bath heats up the entire device from the backside of black PDMS substrate. The in-plane dimensions of the elastomer layer are much larger than its thickness such that the heat flux is mainly along the thickness direction, which can be represented by a one-dimensional heat transfer model described elsewhere. ¹

The sensor response time is defined by the time at which the sensor temperature increase T_{sensor} reaches 90% of T_0 . For 30 μm black PDMS and 25 μm TLC layer as used in the experiment, the response time is predicted to be ~30ms. These agree reasonably well with the experimentally measured sensor response time (for $T_{\text{sensor}} = 0.9T_0$) of 33 ms.

Supplementary Note 6: Color and temperature extraction process

The only parts of TLS sensor that are temperature sensitive are the liquid crystal dots. Finding them in the image and separating from black elastomer background is necessary first stage in temperature extraction process. This is a typical computer vision problem (OpenCV <http://opencv.org/>). The essential steps of the process are illustrated in Fig. 3a. First frame show the original picture of 7x7 area of the sensor array. Second is the output of Gaussian filter which reduce noise through image smoothing. Gray scale (third frame) format is required input for adaptive threshold (fourth frame). Adaptive threshold is the robust algorithm that is aware of the illumination non-uniformity at different parts of the image. The output is the binary mask containing value “1” at bright areas and “0” elsewhere. Small speckles from the defects are visible here as well. They are removed with the two step erode/dilate process. Erode (fifth frame) shrink the white areas in frame four by removing few pixels at the border. Due to the small size of the defects they vanish completely. Dilate step (sixth frame) expand the white regions back restoring area of interest by adding the same amount of pixels removed in the previous step. List of contours can be extracted from this “clean”

image (seventh frame). Every contour is enclosing a single temperature sensitive dot. The shape of the dot is closely reminiscent to circle. The obvious choice for dots position detection is the OpenCV's "enclosing circle" function which take a contour as an input. Last frame is the superposition of the original image and the set of corresponding positions (red dots) and enclosing circles (cyan rings).

Typical output of the digital camera is red-green-blue (RGB) color map. Intensities of all colors are affected by illumination conditions during the experiment. Converting to hue-saturation-value (HSV) color space make analysis more resilient to the change in lightning due to the fact that intensity now is encoded in value channel and color is in hue and saturation channels. In order to track the color change only hue and saturation are of interest. Figure 3b show the calibration we use to convert the colors into temperature. The dots plotted are positioned at corresponding hue/saturation values and painted with their hue value. Background is the temperature evaluated from them with two dimensional linear fit.

Supplementary Note 7: Steady-state thermal conduction model for prediction of thermal conductivity

A Cartesian coordinate system is set such that the origin is located at the center of the top surface of PDMS, as shown in Figs. S8a and S8b, where the schematic illustrations of the device geometry, from both the 3D and cross-sectional views, are presented. FEA indicates that the ultrathin e-TLC dots (~20 μm) have negligible effects on the temperature distributions, and thus are not considered in the analytic model. The skin layer (homogenized from real skin and

the underlying tissues, with the thickness >2 mm) are usually much thicker than the PDMS layer (with a thickness of ~ 60 μm), such that it can be considered as infinitely thick. The steady-state heat conduction equation is $\partial^2 T / \partial x^2 + \partial^2 T / \partial y^2 + \partial^2 T / \partial z^2 = 0$ for both the PDMS and skin, where T is the temperature. The square shaped resistor ($a_{Resistor} \times b_{Resistor}$) serves as the heat source, with the heat generation Q that pumps into the PDMS and skin. This can be modeled as a surface heat flux ($q_0 = Q / (a_{Resistor} b_{Resistor})$) for the bilayer system, i.e., $q_0 = q_{zPDMS}|_{z=-H_{PDMS}} - q_{zSkin}|_{z=-H_{PDMS}}$ for the region occupied by heat source. The free, top surface of the PDMS has natural convection with the surrounding air (T_∞), i.e., $q_{zPDMS}|_{z=0} = h(T - T_\infty)$, with h denoting the heat transfer coefficient. The continuity conditions include $[T]=0$ and $[q_z]=0$ across the PDMS/skin interface, where $[]=0$ stands for the jump across the interface. By adopting the approach of double Fourier transform, the temperature at the sensor plane ($z = -H_{Sensor}$) is obtained as

$$T_{Sensor-layer} = T_\infty + \frac{4q_0}{\pi^2 k_{PDMS}} \cdot \int_0^\infty \cos(\omega x) d\omega \int_0^\infty \frac{\sin \frac{a_{Resistor} \omega}{2} \sin \frac{b_{Resistor} \zeta}{2} \left(e^{\eta H_{Sensor}} + \frac{k_{PDMS} \eta - h}{k_{PDMS} \eta + h} e^{-\eta H_{Sensor}} \right) \cos(\zeta y) d\zeta}{\omega \zeta \eta \left[\left(1 + \frac{k_{Skin}}{k_{PDMS}} \right) e^{\eta H_{PDMS}} - \frac{k_{PDMS} \eta - h}{k_{PDMS} \eta + h} \left(1 - \frac{k_{Skin}}{k_{PDMS}} \right) e^{-\eta H_{PDMS}} \right]} , \quad (3)$$

where the subscripts 'PDMS' and 'skin' denote the PDMS and skin, respectively; k is the thermal conductivity. Eq. (S3) corresponds to the temperature solution of the forward thermal conduction problem, given the thermal conductivity of the skin layer. The parameters adopted in experiments include $a_{Resistor} = b_{Resistor} = 0.5$

mm, $h=5 \text{ W}\cdot\text{m}^{-2}\text{K}^{-1}$, $H_{\text{sensor}}=30 \text{ }\mu\text{m}$, $H_{\text{PDMS}}=60 \text{ }\mu\text{m}$, $k_{\text{PDMS}}=0.16 \text{ W}\cdot\text{m}^{-1}\text{K}^{-1}$, and the thermal diffusivity $\alpha_{\text{PDMS}}=1.07 \text{ m}^2\cdot\text{s}^{-1}$. For a representative value of $k_{\text{skin}}=0.31 \text{ W}\cdot\text{m}^{-1}\text{K}^{-1}$ and $Q=3.8 \text{ mW}$, the distribution of temperature at the sensor plane, as given by Eq. (S3), is shown in Fig. S8c, which agrees reasonably well with FEA results (Fig. S8d). The temperature profile along the x axis (in Fig. S8e) is in quantitative agreement with the FEA results. The relatively large discrepancy at the center region is mainly attributed to the assumption of homogenous heat generation q_0 through the entire heater, adopted for the aim of model simplification. Fig. S8e also shows the temperature gradient is obvious in the region within a distance of $\sim 4 \text{ mm}$ from the heater center. For the sensors far from the heater (0.5 by 0.5 mm), the temperature distribution can be approximated by the simple solution of a point heat source, i.e.,

$$T_{\text{Sensor-layer}} \approx T_{\infty} + \frac{Q}{2\pi k_{\text{skin}} r}, \quad (4)$$

where the ultrathin PDMS layer is neglected, and $r = \sqrt{x^2 + y^2}$ is the in-plane distance from the origin. Fig. S8e demonstrates that this approximate solution has very good accuracy for $r \geq a_{\text{Resistor}}/2$. This simplified solution is adopted to predict the thermal conductivity of skin by fitting the temperature data from the e-TLC device, as shown in Fig. 5a for an example with $T_{\infty} = 33.9 \text{ }^{\circ}\text{C}$ and $Q = 3.83 \text{ mW}$. Fig. 5b demonstrates the prediction of thermal conductivity for the calibration experiment, in which the water/ethylene glycol solutions with different mixing ratios are adopted to mimic real skin in different hydration levels. The

thermal conductivities predicted by the current model agree fairly well with those reported in the literature (MEGlobal, Ethylene Glycol Product Guide).

Supplementary Note 8: Transient thermal conduction model for prediction of thermal diffusivity

To simplify the analyses for the transient thermal conduction problem, we continue to assume that the heater is a point heat source. Consider that the heater is turned on at time $t=0$, the induced transient temperature solution is given by

$$T_{Sensor-layer}(t) \approx T_{\infty} + \frac{Q}{2\pi k_{skin} r} \operatorname{erfc}\left(\frac{r}{\sqrt{4\alpha_{skin} t}}\right), \quad (5)$$

where α_{skin} is the thermal diffusivity of the skin, and $\operatorname{erfc}(x)$ is the complementary error function. For the representative value of $k_{skin}=0.31 \text{ W}\cdot\text{m}^{-1}\text{K}^{-1}$, $\alpha_{skin}=1.14 \text{ m}^2\cdot\text{s}^{-1}$, and $Q=3.8 \text{ mW}$, the time dynamic temperature given by Eq. (S5) agree remarkably well with FEA results, as shown in Fig. S8f, for three different points (with a distance of 0.5, 1.0 and 2.0 mm from the origin).

Based on Eq. (S5), we can determine the thermal diffusivity based on the transient temperature data from the e-TLC device, even when the power is unknown (e.g., when the wireless system is adopted to power the heater). Fig. 5d gives an example of temperature profile at the sensor with a distance of 0.5 mm from the heater, where the analytic curve with the thermal diffusivity of $0.43 \times 10^{-7} \text{ m}^2/\text{s}$ gives the best match with the experimental data. Fig. 5e demonstrates the predictions of thermal diffusivity for the calibration experiment,

which agree reasonably well with those reported in the literature (MEGlobal, Ethylene Glycol Product Guide).

Supplementary Note 9: Mathematical modeling of reactive hyperemia

A two-dimensional (2D), transient, heat transfer model of human wrist was developed, which considers the various tissues surrounding the ulnar artery, and quantitatively characterizes the heat exchange between the blood flow and the surrounding tissues. Figure S10a and S10b show the schematic illustration of the tissue geometry, in which a circular cross section is adopted for the wrist to simplify the analyses. The blood at body temperature flows through the circular artery embedded in the fat layer, heating the surrounding tissues. The heat exchange between the blood flow and the fat layer across the artery wall is described with a heat convection model ², which assumes the exchanged heat flux (q) to be proportional to the blood flow rate, i.e.

$$q = \frac{\rho_b c_{pb} \omega_b(t)}{\pi D_{artery}} (T_{body} - T_s), \quad (6)$$

where ρ_b , c_{pb} , $\omega_b(t)$ are the density, specific heat capacity, and time-dependent flow rate of the blood; D_{artery} is the diameter of the artery; T_{body} and T_s are the body temperature, and the temperature of fat at the artery wall, respectively. Due to the heating of the blood flow, the temperature distributes non-uniformly in these tissues, which is governed by the temporal heat conduction equation of

$$\rho_j c_j \frac{\partial T_j}{\partial t} = k_j \left(\frac{\partial^2 T_j}{\partial x^2} + \frac{\partial^2 T_j}{\partial y^2} + \frac{\partial^2 T_j}{\partial z^2} \right) \quad (j=1..4),$$

with the subscript representing different tissues (with skin as $j=1$, fat as $j=2$, muscle as $j=3$, and bone as $j=4$). The free,

outer surface of the skin has natural convection with air, which usually cools down the skin due to a lower room temperature than body temperature. The interior bone layer is assumed to maintain the core-temperature (close to the body temperature T_{body}).

The modeling of occlusion involves two steps, starting from the simulation of the steady-state heat conduction in the various tissues due to constant heating of blood flow, corresponding to the stage of pre-occlusion (Stage I). With the steady-state solution as an input, we further simulate the temporal changes in temperature distributions due to the application and release of occlusion, corresponding to the stage of vascular occlusion (Stage II) and reperfusion (Stage III), respectively. Based on previous experimental data, the temporal variation of blood flow during these different stages can be well described by the following piecewise function ^{2,3}

$$\begin{aligned}
 \omega_b^I(t) &= \omega_0, \quad t \leq t_{occ,st} \\
 \omega_b^{II}(t) &= (\omega_0 - \omega_s) \exp(-t/\tau_0) + \omega_s, \quad t_{occ,st} < t \leq t_{occ,end} \\
 \omega_b^{III}(t) &= \begin{cases} (\omega_{max} - \omega_s) \sin^2 \left[\pi (t - t_{occ,end}) / (2t_{dw}) \right] + \omega_s, & t_{occ,end} < t \leq (t_{occ,end} + t_{dw}) \\ (\omega_{max} - \omega_f) \exp \left[-(t - t_{occ,end} - t_{dw}) / \tau_h \right] + \omega_0, & t > (t_{occ,end} + t_{dw}) \end{cases}
 \end{aligned} \tag{7}$$

where ω_0 represents the baseline blood flow; ω_s is the blood perfusion after the occlusion is applied for a sufficiently long time, 160 s in the case of experiments here; ω_{max} is the maximum hyperemic blood flow; τ_0 is a time constant depicting the falling speed of blood flow after occlusion is applied; t_{dw} is the time required to reach the maximum hyperemic blood flow after the release of occlusion; τ_h indicates the rate at which the blood flow returns to the baseline value during the reperfusion; $t_{occ,st}$ and $t_{occ,end}$ denote the starting and ending times of the

occlusion, respectively. Except for $t_{occ,st}$ and $t_{occ,end}$, which are known in experiments ($t_{occ,st}=0$ s, $t_{occ,end}=160$ s), there are six parameters in this model of reactive hyperemia which can be varied to simulate the temperature history of blood perfusion. The aim of the thermal analyses is to obtain an optimized set of parameters that can minimize the average difference between the simulations and experiment data of temperature-time profile at those sensors with a distance ≤ 7 mm from the artery (Fig. 6g). The baseline blood flow ω_0 does not involve the occlusion process, and therefore can be determined using the temperature value measured before the occlusion (Stage I). The blood flow ω_s and time parameter τ_0 (only related to Stage II) are determined by the measured temperature-time profile during Stage II, and the other three parameters (ω_{max} , t_{dw} and τ_h) are determined by the data during Stage III. In total, there are six parameters in our simulations, i.e., ω_0 , $\alpha=\omega_s/\omega_0$, $\beta=\omega_{max}/\omega_0$, τ_0 , t_{dw} and τ_h , whose ranges are listed in Supplementary Table 1, based on reported experiments^{2,3}

Finite element analyses (FEA) were adopted to solve the above transient heat transfer equation, and determine the temperature distribution numerically. 4-node linear heat transfer elements were used, and refined meshes were adopted to ensure the accuracy. The boundary conditions include the prescribed temperature ($T=T_{body}$) in the bone layer, the heat convection at the artery wall with blood flow of body temperature (i.e., Eq. (S6)), and the natural convection at the outer surface of skin with air of room temperature (~ 27.0 °C). The geometric and thermal-physical properties of various tissues are given in Supplementary Table 2. For the reactive hyperemia model described above, the baseline blood

flow rate is determined as $\omega_0=30$ mL/min (19.6 cm/s for a vessel diameter of 1.8 mm), which could minimize the difference between FEA and experiment, i.e., the variance, as shown in Fig. S10c. Based on $\omega_0=30$ mL/min, the calculated temperature decay from the artery at the steady state indeed agree well with experiment data (Fig. S10d). To minimize the temperature variance during stage II (Fig. S10e), the blood flow ω_s and time parameter τ_0 are determined as $\omega_s=1.5$ mL/min and $\tau_0=2$ s. Similarly, the other three parameters corresponding to stage III can be obtained as $\omega_{\max}=90$ mL/min (58.8 cm/s), $t_{dw}=15$ s and $\tau_h=35$ s. For this set of parameters, the temperature-time profile obtained from FEA agrees reasonably well with the experiment results (Fig. 6g) for all the sensor points close to the artery.

Supplementary References

- 1 Webb, R. C. *et al.* Ultrathin conformal devices for precise and continuous thermal characterization of human skin. *Nat. Mater.* **12**, 938 (2013).
- 2 Deshpande, C. *Thermal analysis of vascular reactivity MS thesis*, Texas A&M University, (2007).
- 3 Akhtar, M. W., Kleis, S. J., Metcalfe, R. W. & Naghavi, M. Sensitivity of digital thermal monitoring parameters to reactive hyperemia. *J. Biomech. Eng-T. Asme.* **132**, 051005 (2010)
- 4 Fiala, D., Lomas, K. J. & Stohrer, M. A computer model of human thermoregulation for a wide range of environmental conditions: The passive system. *J. App. Physiol.* **87**, 1957-1972 (1999).
- 5 Song, W. J., Weinbaum, S., Jiji, L. M. & Lemons, D. A combined macro and microvascular model for whole limb heat transfer. *J. Biomech. Eng-T. Asme.* **110**, 259-268 (1988).
- 6 Sieg, P., Hakim, S. G., Bierwolf, S. & Hermes, D. Subcutaneous fat layer in different donor regions used for harvesting microvascular soft tissue flaps in slender and adipose patients. *Int. J. Oral. Max. Surg.* **32**, 544-547 (2003).
- 7 Shen, H. *et al.* A genomewide scan for quantitative trait loci underlying areal bone size variation in 451 Caucasian families. *J. Med. Genet.* **43**, 873-880 (2006).
- 8 Shima, H., Ohno, K., Michi, K. I., Egawa, K. & Takiguchi, R. An anatomical study on the forearm vascular system. *J. Cranio. Maxill. Surg.* **24**, 293-299 (1996).
- 9 McCartney, C. J. L., Xu, D., Constantinescu, C., Abbas, S. & Chan, V. W. S. Ultrasound Examination of Peripheral Nerves in the Forearm. *Region. Anesth. Pain. M.* **32**, 434-439 (2007).
- 10 Kathirgamanathan, A., French, J., Foxall, G. L., Hardman, J. G. & Bedford, N. M. Delineation of distal ulnar nerve anatomy using ultrasound in volunteers to identify an optimum approach for neural blockade. *Eur. J. Anaesth.* **26**, 43-46 (2009).